Supplementary Information

Dual pH-responsiveness pseudopeptide: hydrogelation and self-assembly into single- and multi-walled nanotubes.

Arturo Blanco-Gómez,*[a,b] Liliana Barravecchia,[b] Erica Scarel,[a] Rita De Zorzi,[a] Laura Colomina-Alfaro,[c] Antonella Bandiera,[c] Slavko Kralj,[d,e] Alejandro Vila,[b] Davide Porrelli,[c] Carlos Peinador,[b] Marcos D. García,*[b] Silvia Marchesan*[a]

[a] Chem. Pharm. Sc. Dept., University of Trieste, 34127 Trieste, Italy

[b] Interdisc. Ctr. Chem. & Biol. (CICA) and Chemistry Dept., Faculty of Science, University of Coruña, 15071 A Coruña, Spain

[c] Life Science Dept., University of Trieste, 34127 Trieste, Italy

[d] Materials Synthesis Dept., Jožef Stefan Institute, 1000 Ljubljana, Slovenia

[e] Dept. of Pharmaceutical Technology, Faculty of Pharmacy, University of Ljubljana, 1000 Ljubljana, Slovenia

email: arturo.blanco.gomez@udc.es, marcos.garcia1@udc.es, smarchesan@units.it

Table of Contents:

S1. General methods.

All reagents and solvents were purchased from commercial supplies and used without further purification. Compound **1**·I was synthetized according to the literature.[1] NMR spectra were recorder on a Bruker ADVANCE 500 equipped with dual $^{1}H/^{13}C$ cryoprobe and operating at 500 and 126 MHz for ^{1}H and ^{13}C respectively, Bruker ADVANCE III HD 400 equipped with BBFO probe for broadband observation and operating at 400 and 101 MHz for ^{1}H and ^{13}C respectively, and Varian Innova operating at 376 MHz for ^{19}F. The NMR solvents used were deuterated water (D_2O), and dimethylsulfoxide-d6 (DMSO-d6). Chemical shifts are reported in ppm relative tetramethylsilane (TMS, δ = 0 ppm) or, otherwise, to the residual internal non deuterated solvent signal (D_2O, δ = 4.79 ppm, DMSO-d6, δ = 2.50 ppm). High-resolution mass spectrometry experiments were carried out in a ESI-TOF LTQ-Orbitrap Discovery mass spectrometer.

[1] Blanco-Gomez, A.; Neira, I.; Barriada, J. L.; Melle-Franco, M.; Peinador, C.; Garcia, M. D., Thinking outside the "Blue Box": from molecular to supramolecular pH-responsiveness. *Chem. Sci.* **2019**, *10*, 10680-10686.

S2. Synthesis and Characterization of 2·Br.

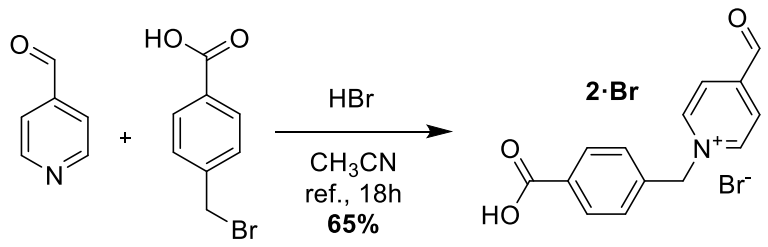

To a solution of isonicotinaldehyde (375 mg, 330 µL, 3.5 mmol) and 4-(chloromethyl)benzoic acid (688 mg, 3.2 mmol) in 30 mL of acetonitrile, HBr (0.1 mL, 2 mmol, 48 %) was added dropwise at room temperature. The solution was heated to reflux for 18 hours in a magnetic hot plate stirrer. The resulting precipitate was filtered and washed with hot acetonitrile (3 x 15 mL) and dried under vacuum, yielding compound **2·Br** as a yellow solid (670 mg, 65 %).

^{1}H NMR (400 MHz, D_2O) δ 8.97 (d, J = 6.9 Hz, 2H), 8.20 (d, J = 6.7 Hz, 2H), 8.09 (d, J = 8.4 Hz, 2H), 7.57 (d, J = 8.5 Hz, 2H), 6.24 (s, 1H), 5.94 (s, 2H) ppm. **^{13}C NMR** (101 MHz, D_2O) δ 169.93 (CO_2H), 160.53 (C_{Py}), 144.88 (CH_{Py}), 137.79 (C_{Ph}), 131.16 (C_{Ph}), 130.58 (CH_{Ph}), 128.97 (CH_{Ph}), 125.67 (CH_{Py}), 87.53 ($CH(OH)_2$), 63.65 (CH_2) ppm. **HR-MS (ESI)** (*m/z*): calcd for $[M+MeOH]^+$ = 274.1074, found 274.1071; calcd for $[M]^+$ = 242.0812, found 242.0809.

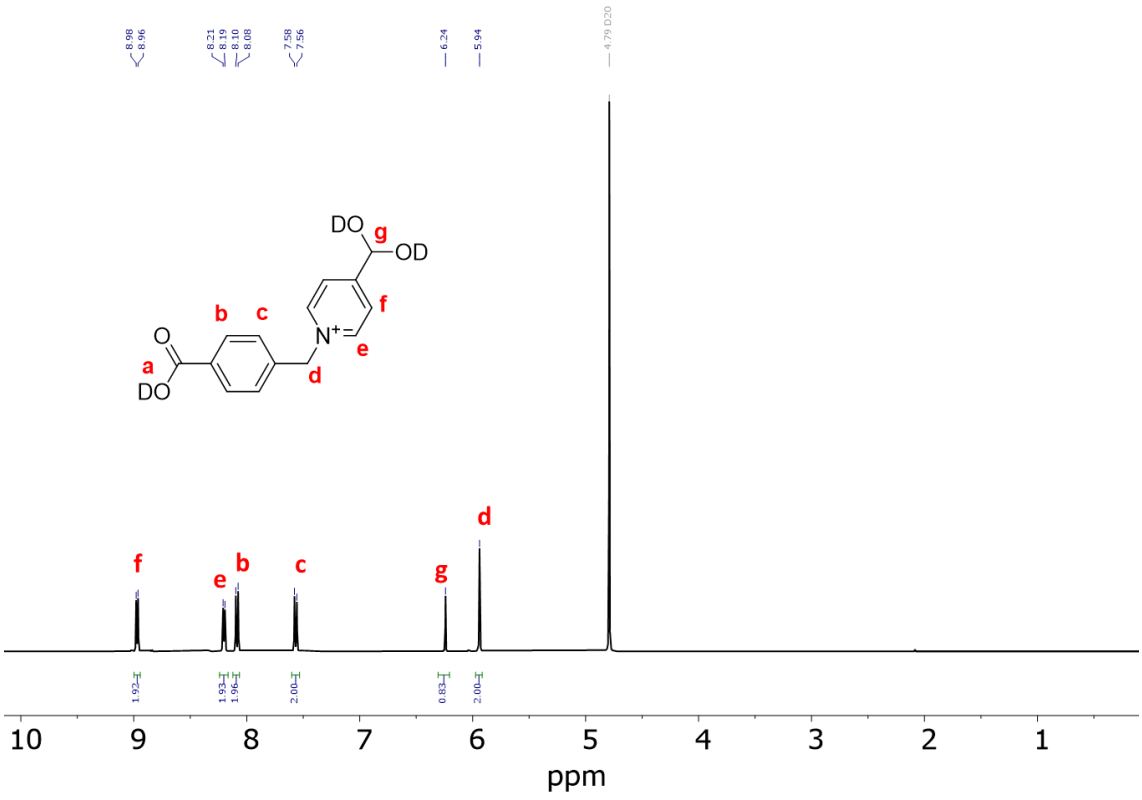

Fig. S1. ^{1}H-NMR (400 MHz, D_2O) spectrum of **2·Br**.

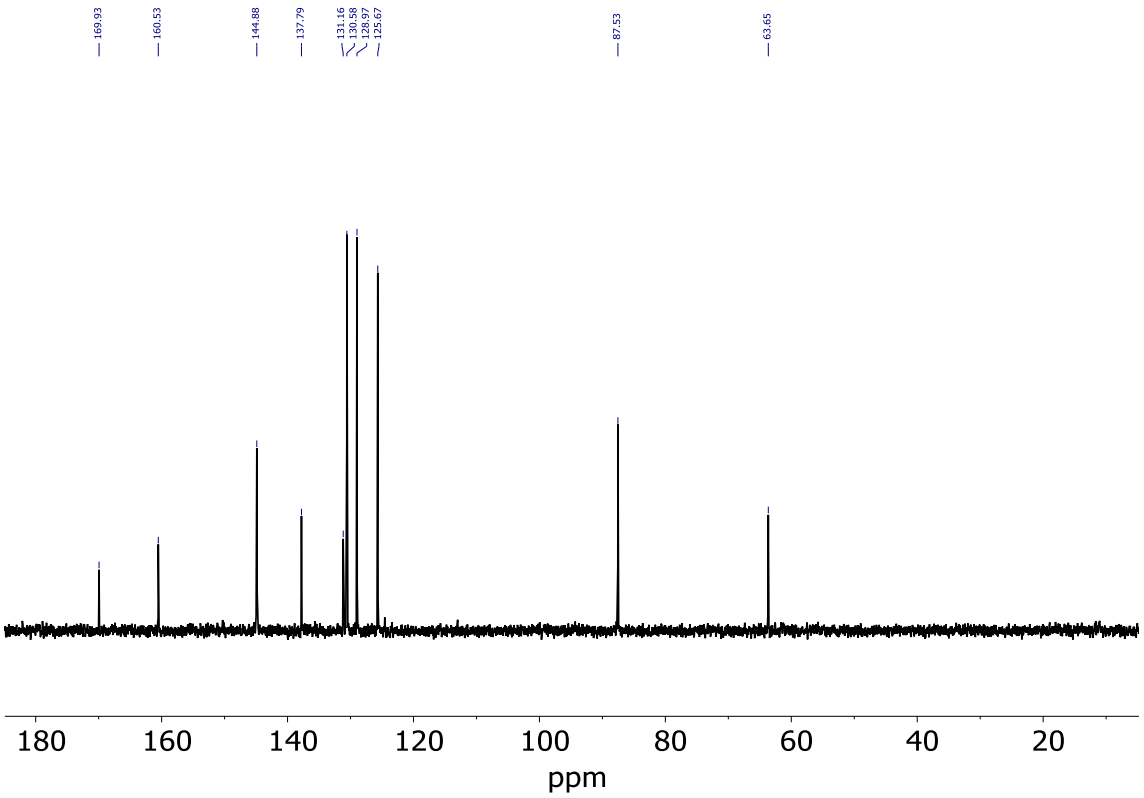

Fig. S2. ^{13}C-NMR (101 MHz, D_2O) spectrum of **2·Br**.

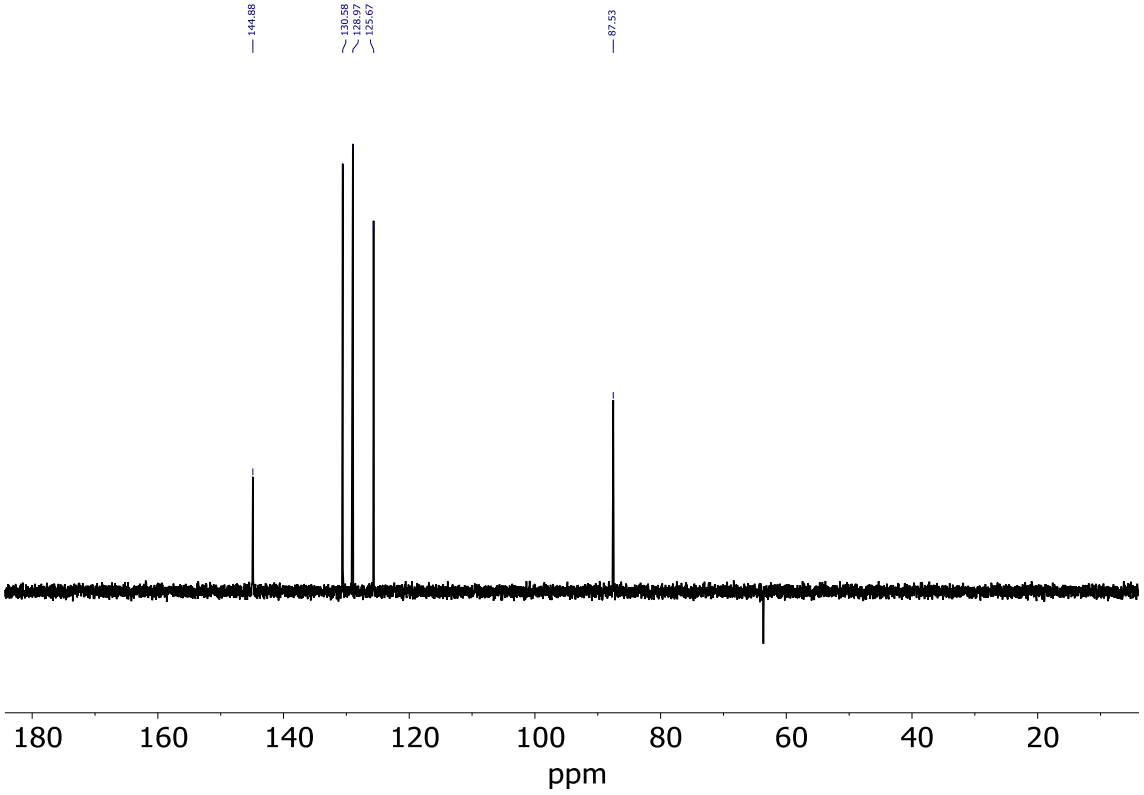

Fig. S3. DEPT-135 (101 MHz, D_2O) spectrum of **2·Br**.

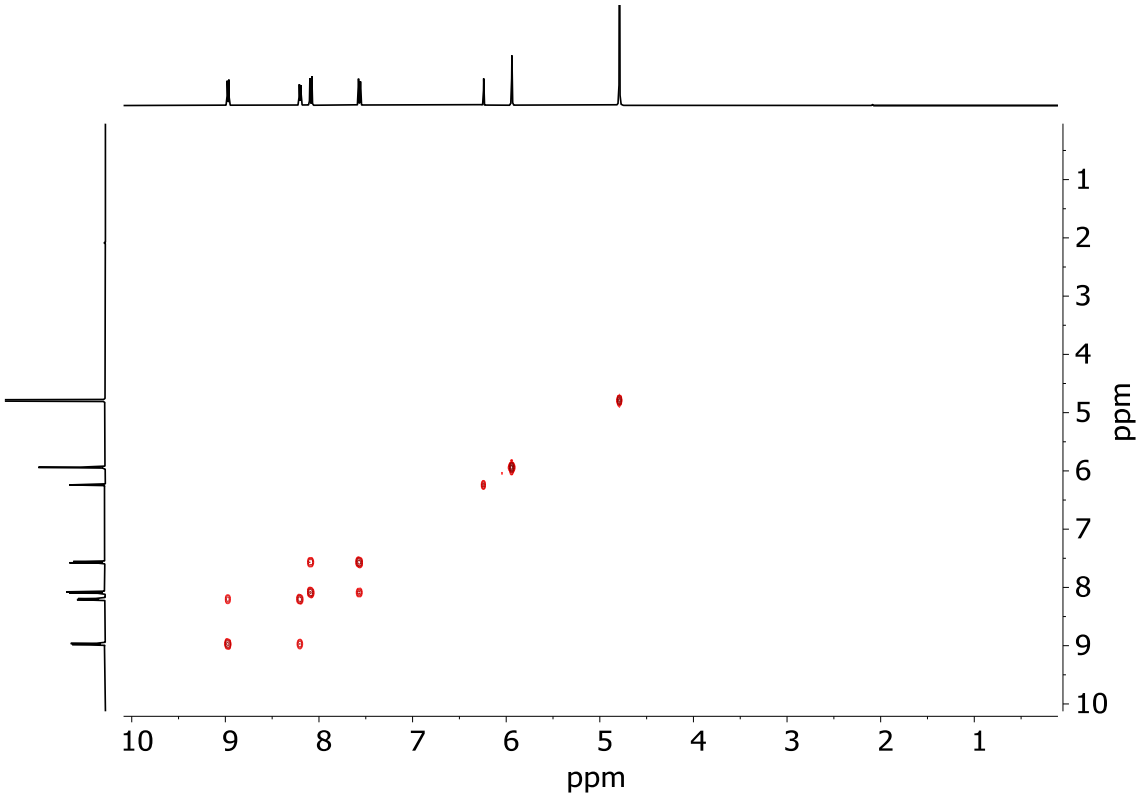

Fig. S4. ^{1}H-^{1}H COSY (400 MHz, D_2O) spectrum of **2·Br**.

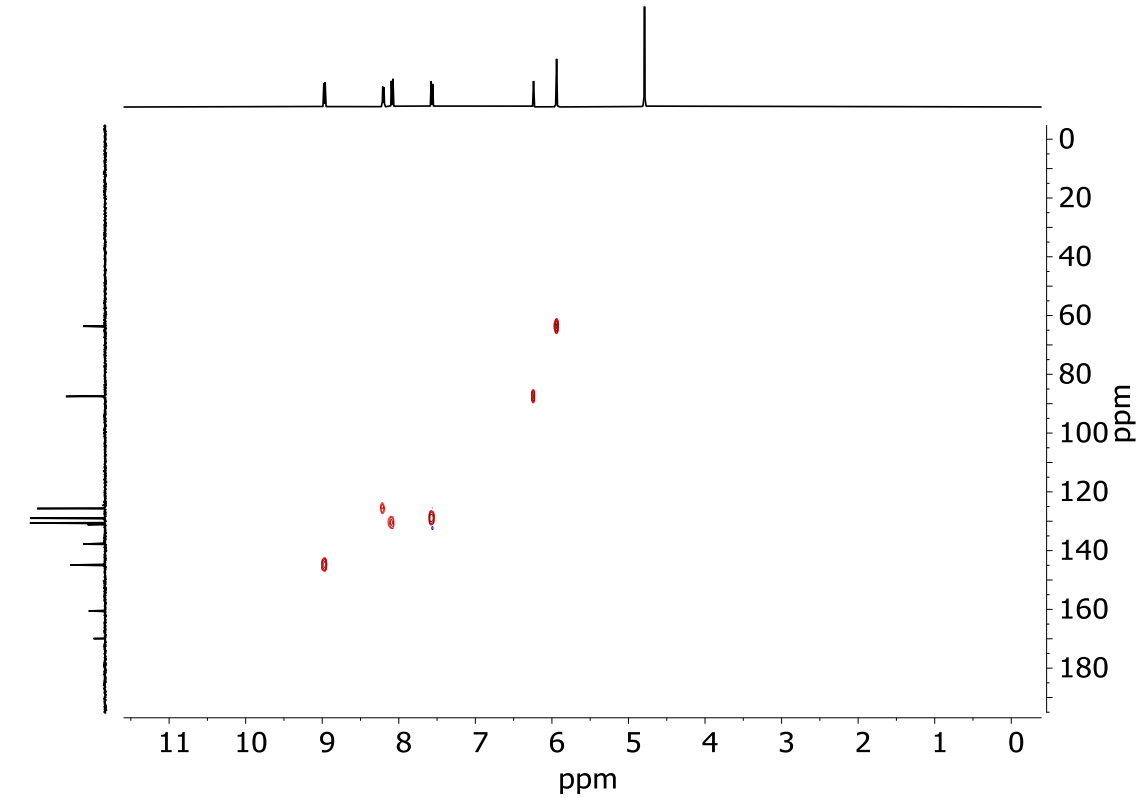

Fig. S5. ^{1}H-^{13}C HSQC (400 and 101 MHz, D_2O) spectrum of **2·Br**.

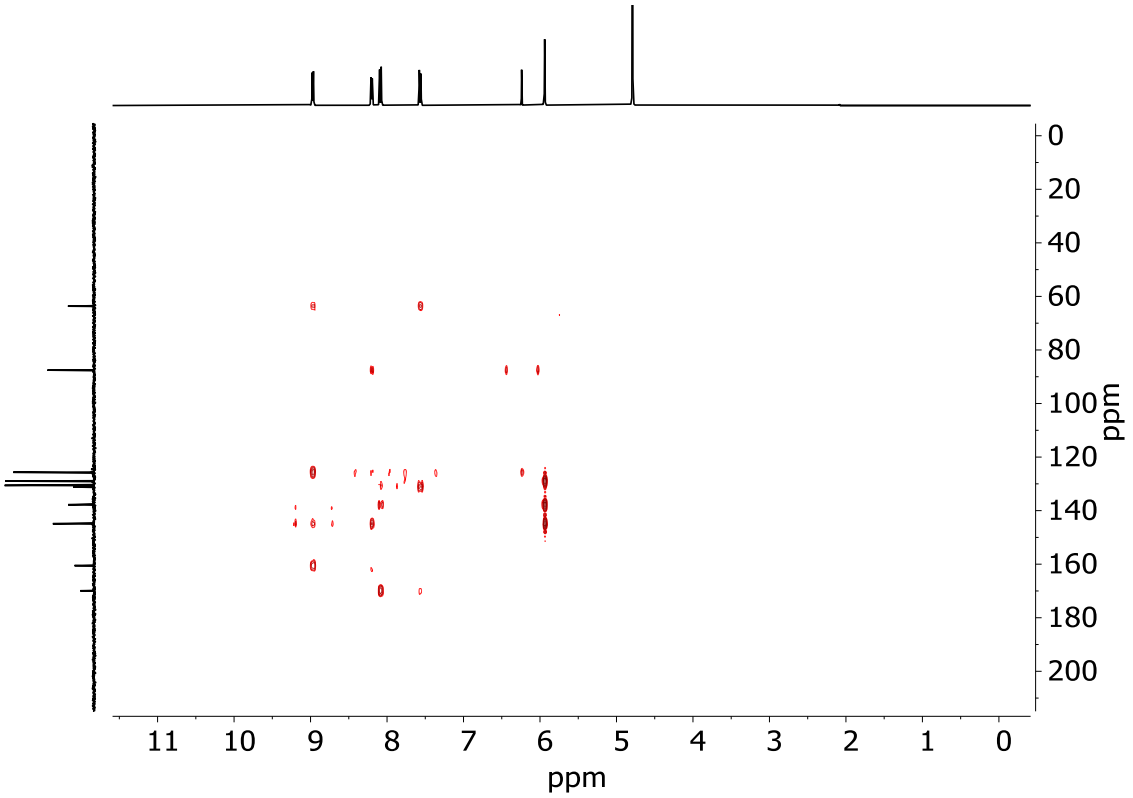

Fig. S6. ^{1}H-^{13}C HMBC (400 and 101 MHz, D_2O) spectrum of **2·Br**.

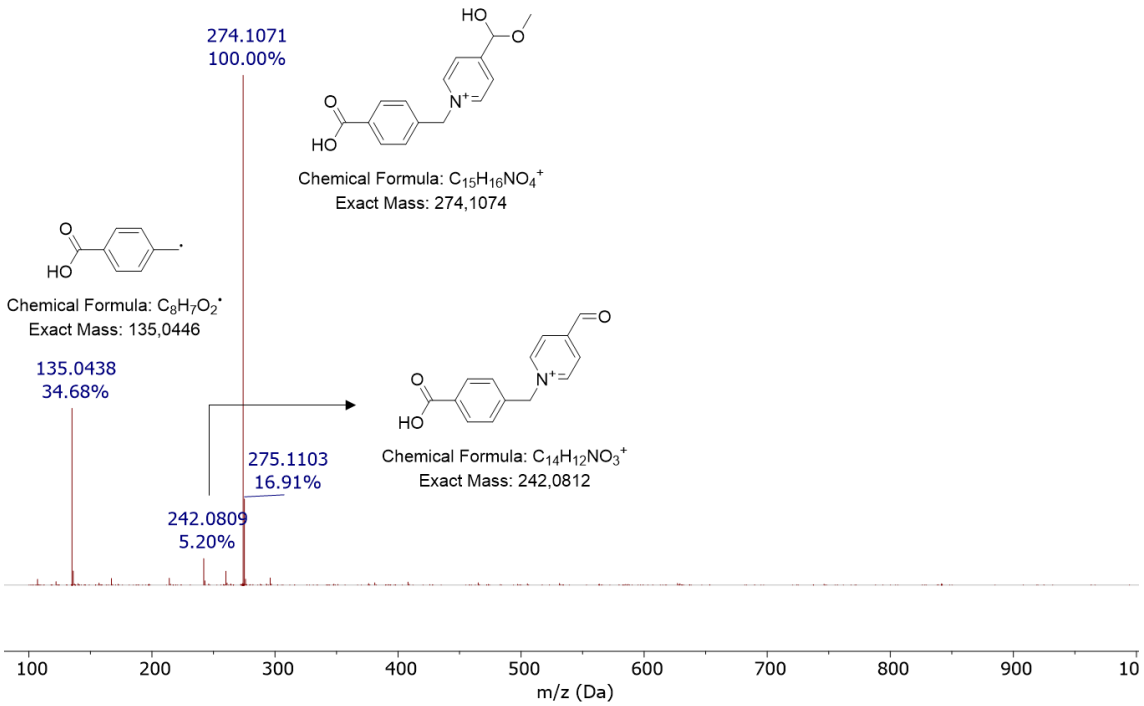

Fig. S7. ESI-HRMS spectrum of **2·Br**.

S3. Synthesis and Characterization of V·2PF$_6$.

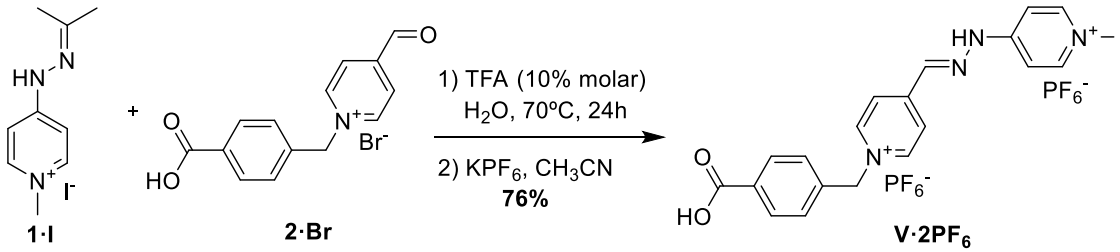

A solution of **1**·I (457 mg, 1.57 mmol), **2**·Br (506 mg, 1.57 mmol) and TFA (10% molar) in 150 mL of water were heated at 70ºC for 24 hours in a magnetic hot plate stirrer. After cooling, excess of KPF_6 were added until no further precipitation was observed. The resulting precipitate was filtered, washed with water (3 x 10 mL) and Et_2O (3 x 10 mL), and dried under vacuum, yielding compound **V**·2PF6 as a white solid (765 mg, 76%).

^{1}H NMR (500 MHz, DMSO-d6) δ 12.92 (s, 1H), 9.19 (d, J = 6.7 Hz, 2H), 8.55 (d, J = 6.9 Hz, 2H), 8.51 (s, 2H), 8.33 (s, 1H), 8.00 (d, J = 8.4 Hz, 2H), 8.00 (s, 1H) 7.60 (d, J = 8.5 Hz, 2H), 7.26 (s, 1H), 5.92 (s, 2H), 4.09 (s, 3H) ppm. **^{13}C NMR** (126 MHz, DMSO-d6) δ 166.14 (CO_2H), 153.07 (C_{Py}), 148.86 (C_{Py}), 144.85 (CH_{Py}), 144.57 (CH_{Py}), 140.28 (CH=N), 138.38 (C_{Ph}), 130.87 (C_{Ph}), 129.46 (CH_{Ph}), 128.03 (CH_{Ph}), 124.42 (CH_{Py}), 109.54 (CH_{Py}), 108.06 (CH_{Py}), 61.73 (CH_2), 44.89 (CH_3) ppm. **HR-MS (ESI)** (*m*/*z*): calcd for $[M]^+$ = 347.1503, found 347.1504.

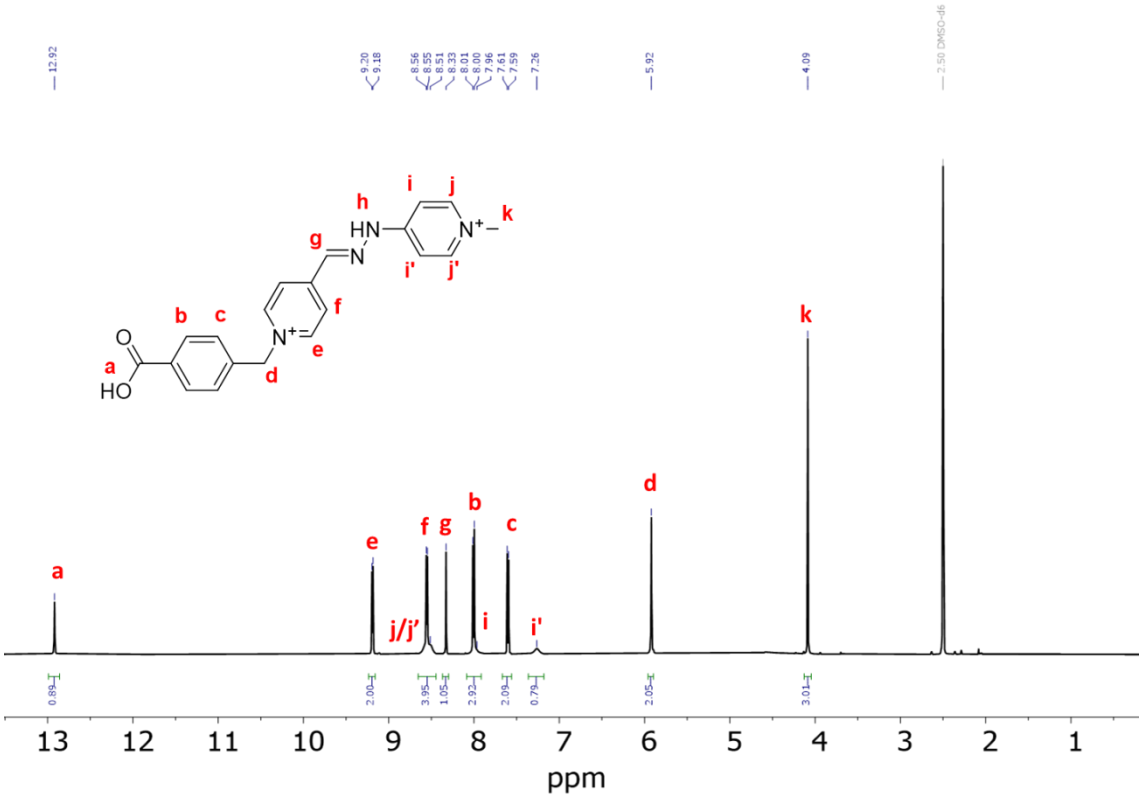

Fig. S8. ^{1}H-NMR (500 MHz, DMSO-d6) spectrum of **V·2PF$_6$**.

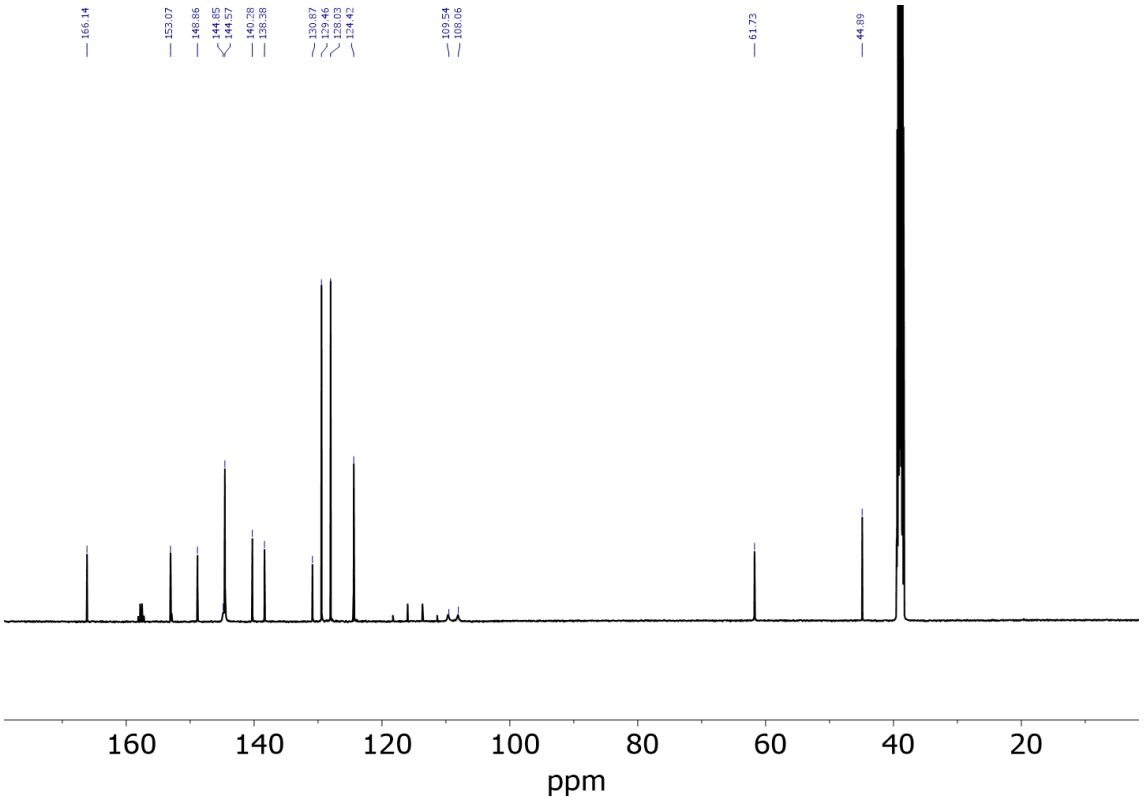

Fig. S9. ^{13}C-NMR (126 MHz, DMSO-d6) spectrum of **V·2PF$_6$**.

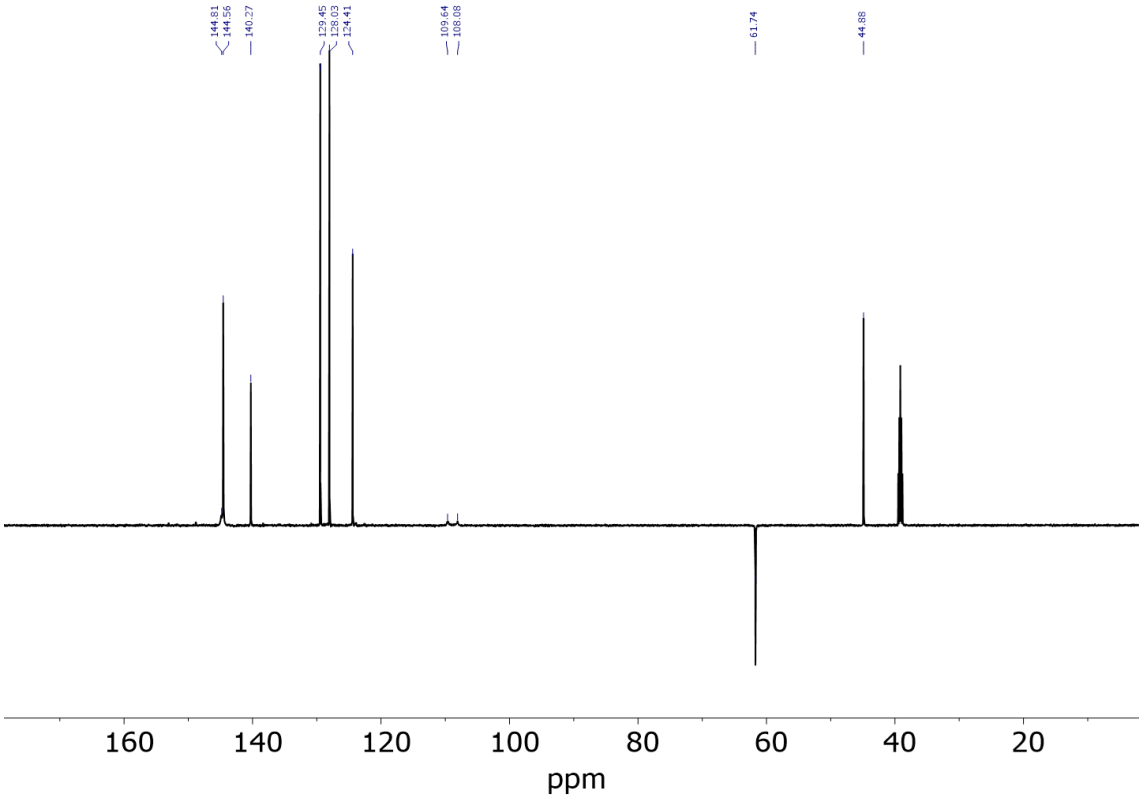

Fig. S10. DEPT-135 (126 MHz, DMSO-d6) spectrum of **V·2PF$_6$**.

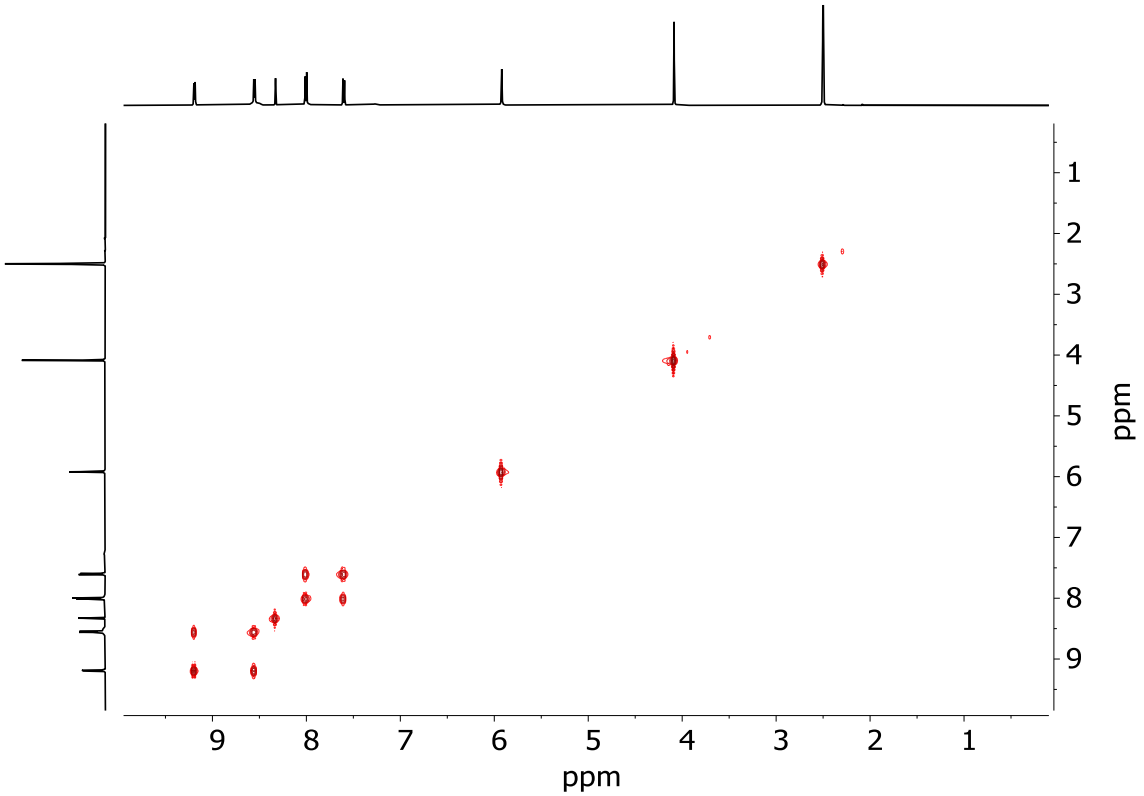

Fig. S11. ^{1}H-^{1}H COSY (500 MHz, DMSO-d6) spectrum of **V·2PF$_6$**.

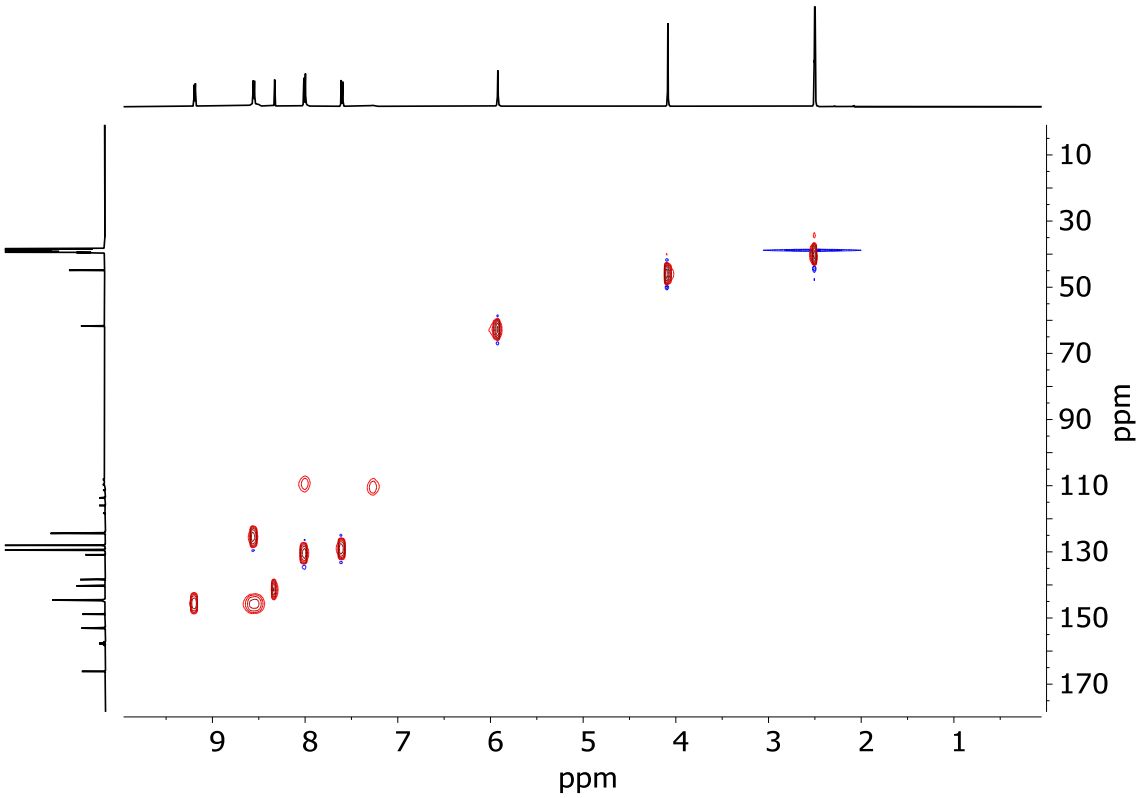

Fig. S12. ^{1}H-^{13}C HSQC (500 and 126 MHz, DMSO-d6) spectrum of **V·2PF$_6$**.

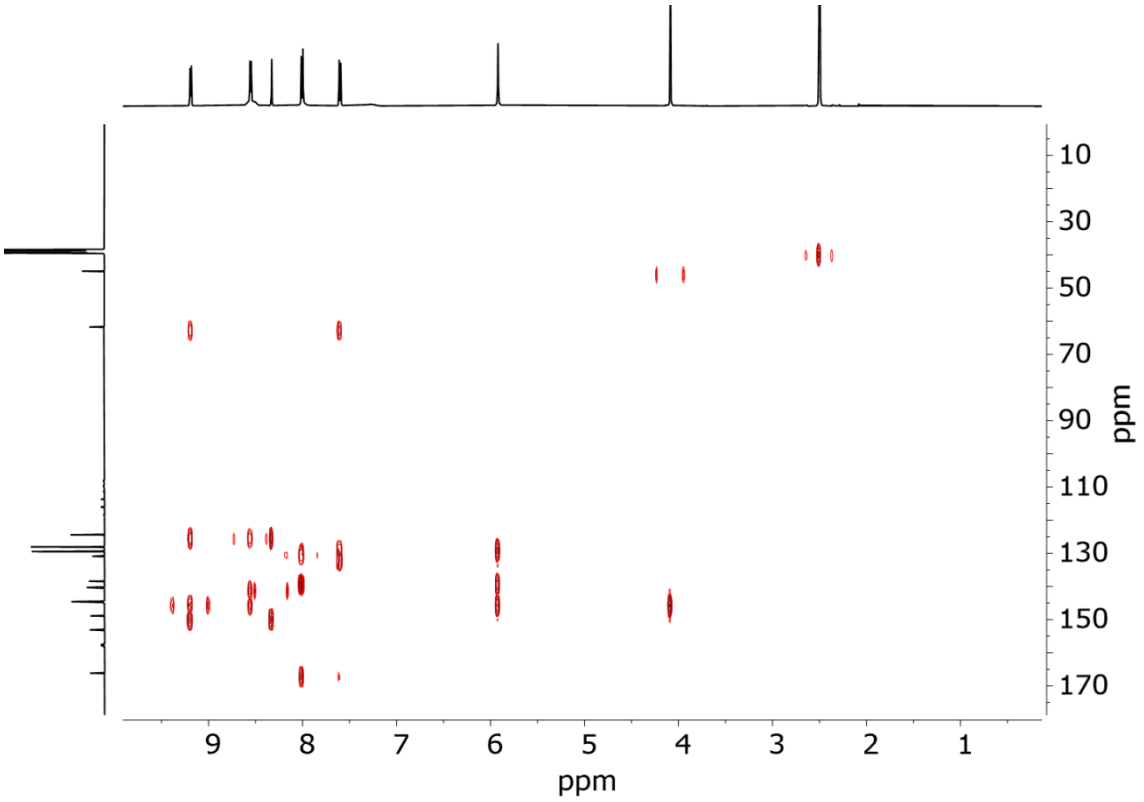

Fig. S13. ^{1}H-^{13}C HMBC (500 and 126 MHz, DMSO-d6) spectrum of **V·2PF$_6$**.

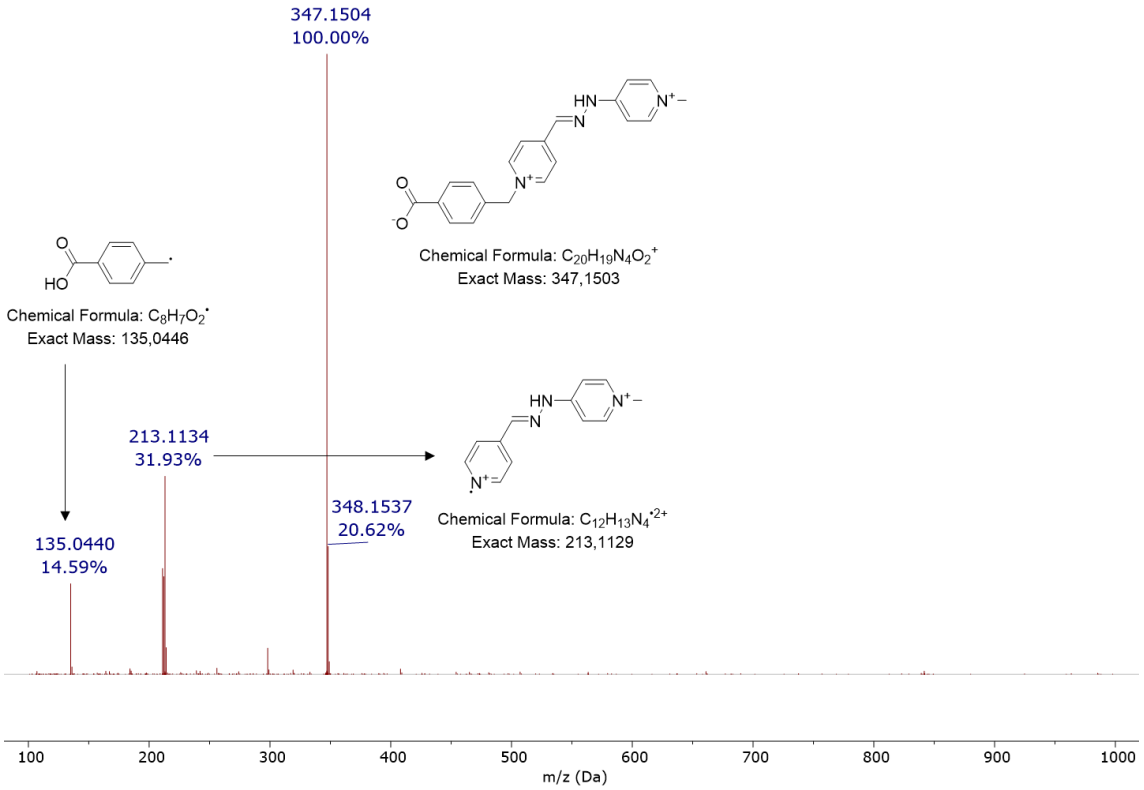

Fig. S14. ESI-HRMS spectrum of **V·2PF$_6$**.

S4. Characterization data of V-FfF/fFH$_2$·2TFA.

Spectroscopic data for V-fFH$_2$·2TFA:

^{1}H NMR (500 MHz, DMSO-d6) δ 13.14 (s, 1H), 12.90 (br, 1H), 9.18 (d, J = 6.8 Hz, 2H), 8.57 (s, 1H), 8.55 – 8.51 (m, 5H), 8.36 (s, 1H), 7.83 (d, J = 8.2 Hz, 2H), 7.55 (d, J = 8.2 Hz, 2H), 7.29 – 7.06 (m, 11H), 5.87 (s, 2H), 4.73 (ddd, J = 11.0, 8.7, 3.8 Hz, 1H), 4.52 (ddd, J = 9.9, 8.4, 4.6 Hz, 1H), 4.09 (s, 3H), 3.11 (dd, J = 13.7, 4.6 Hz, 1H), 2.87 (dd, J = 13.8, 9.8 Hz, 1H), 2.77 (dd, J = 13.7, 3.8 Hz, 1H), 2.68 (dd, J = 13.7, 11.1 Hz, 1H). **^{13}C NMR** (126 MHz, DMSO-d6) δ 172.76 (CO_2H), 171.02 (C=O), 165.10 (C=O), 153.62 (C_{Py}), 149.28 (C_{Py}), 145.42 (CH_{Py}), 144.97 (CH_{Py}), 140.79 (CH=N), 138.19 (C_{Ph}), 137.30 (C_{Ph}), 137.26 (C_{Ph}), 134.51 (C_{Ph}), 129.18 (CH_{Ph}), 129.01 (CH_{Ph}), 128.23 (CH_{Ph}), 128.00 (CH_{Ph}), 127.99 (CH_{Ph}), 127.83 (CH_{Ph}), 126.35 (CH_{Ph}), 126.04 (CH_{Ph}), 124.85 (CH_{Ph}), 110.24 (CH_{Py}), 108.64 (CH_{Py}), 62.23 (CH_2), 54.51 (CH), 53.13 (CH), 45.35 (CH_3), 37.19 (CH_2), 37.03 (CH_2). **HR-MS (ESI)** (m/z): calcd for $[M]^+$ = 641.2871, found 641.2872.

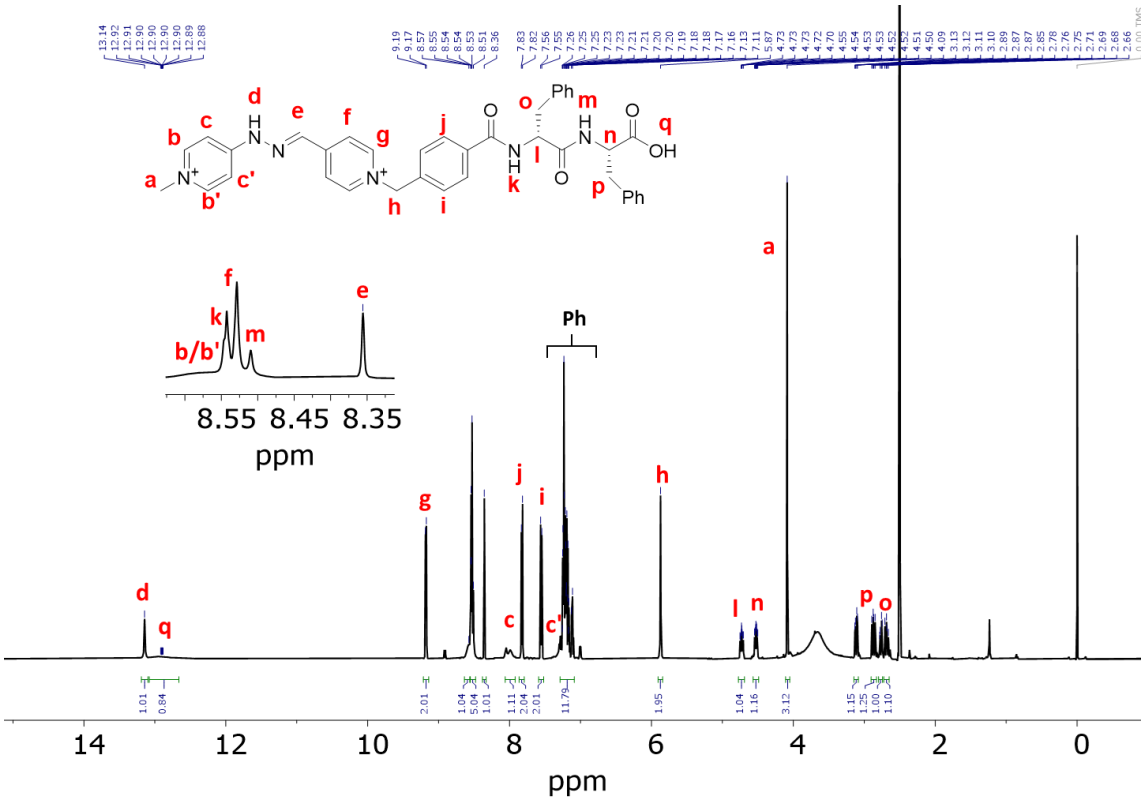

Fig. S15. ^{1}H-NMR (500 MHz, DMSO-d6) spectrum of **V-fFH$_2$·2TFA**.

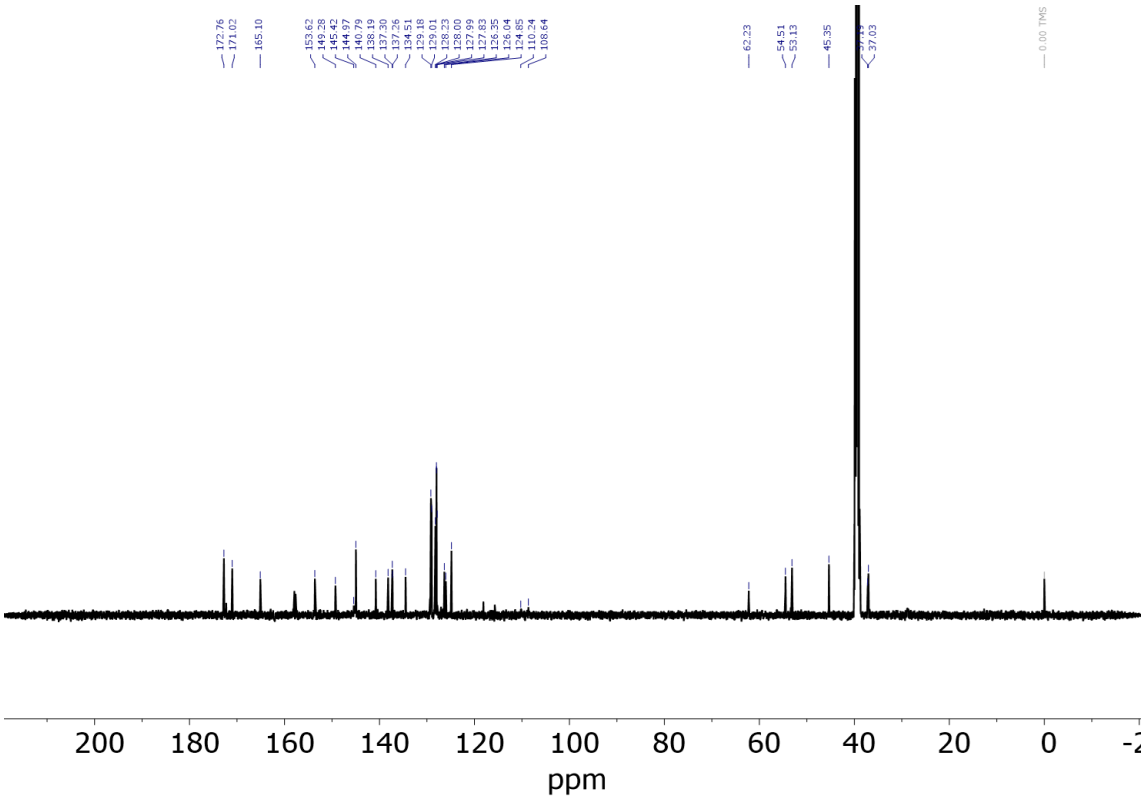

Fig. S16. ^{13}C-NMR (126 MHz, DMSO-d6) spectrum of **V-fFH$_2$·2TFA**.

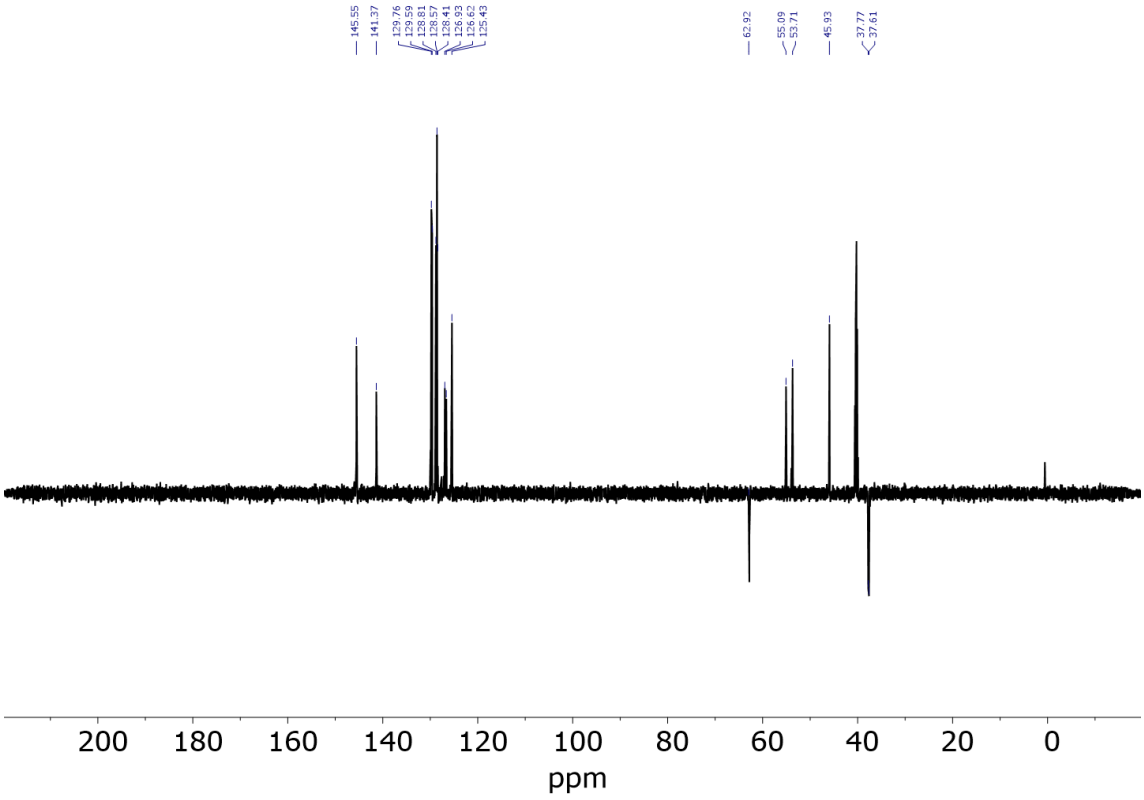

Fig. S17. DEPT-135 (126 MHz, DMSO-d6) spectrum of **V-fFH$_2$·2TFA**.

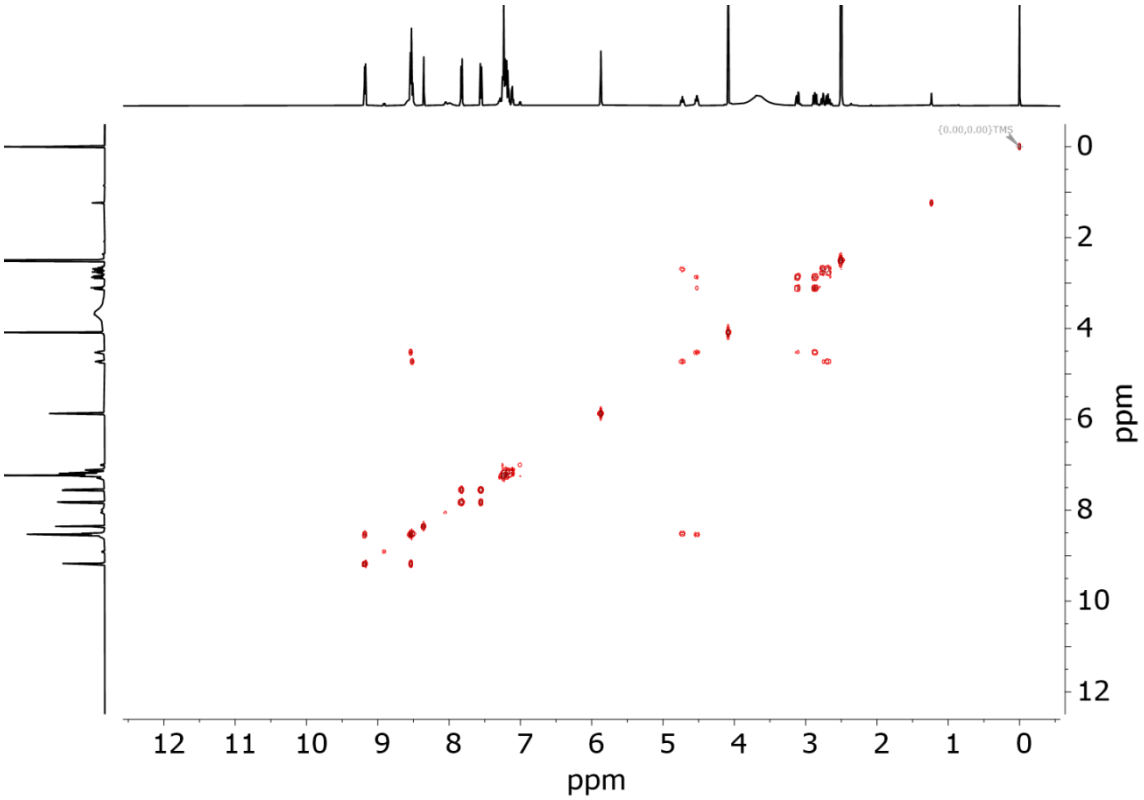

Fig. S18. ^{1}H-^{1}H COSY (500 MHz, DMSO-d6) spectrum of **V-fFH$_2$·2TFA**.

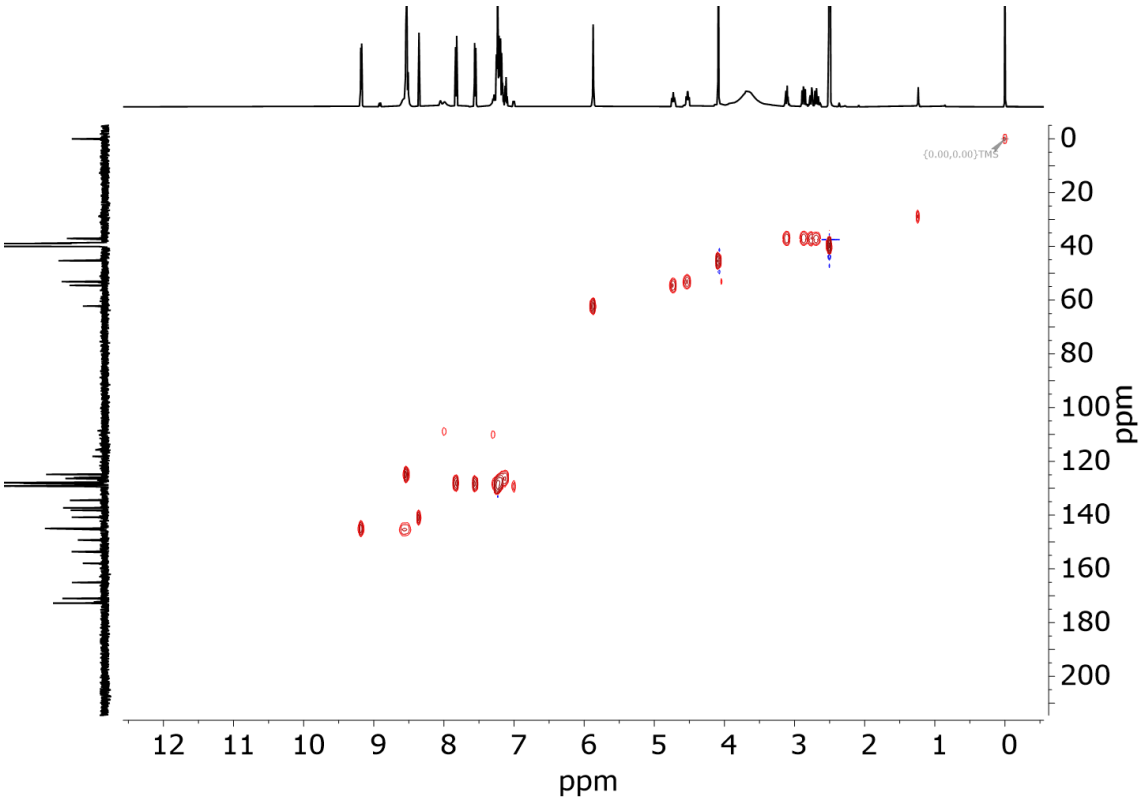

Fig. S19. ^{1}H-^{13}C HSQC (500 and 126 MHz, DMSO-d6) spectrum of **V-fFH$_2$·2TFA**.

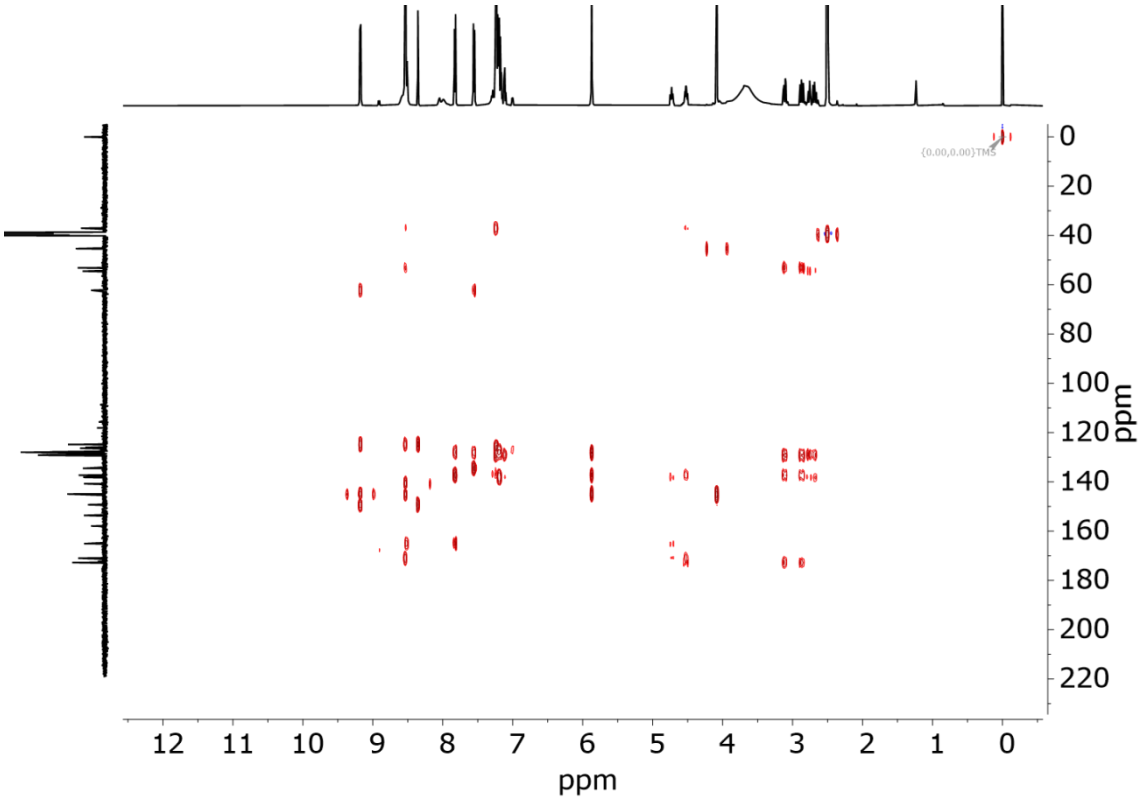

Fig. S20. ^{1}H-^{13}C HMBC (500 and 126 MHz, DMSO-d6) spectrum of **V-fFH$_2$·2TFA**.

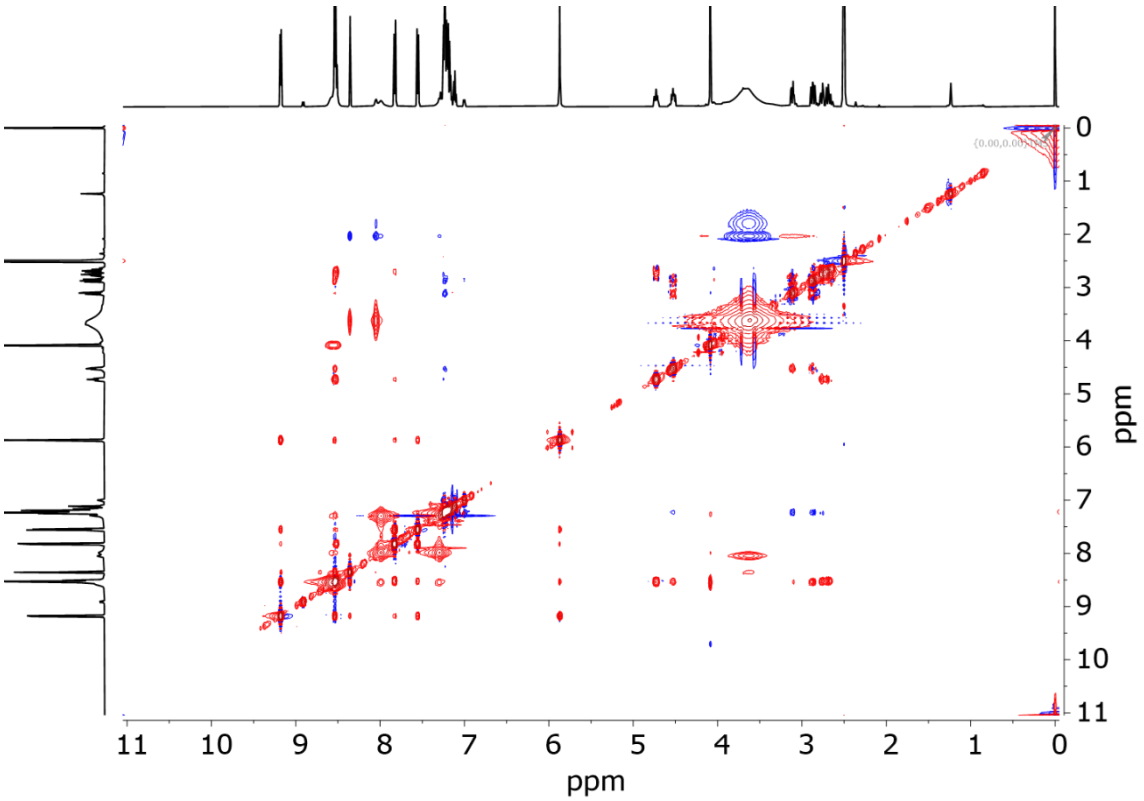

Fig. S21. ^{1}H-^{1}H NOESY (500 MHz, DMSO-d6) spectrum of **V-fFH$_2$·2TFA**.

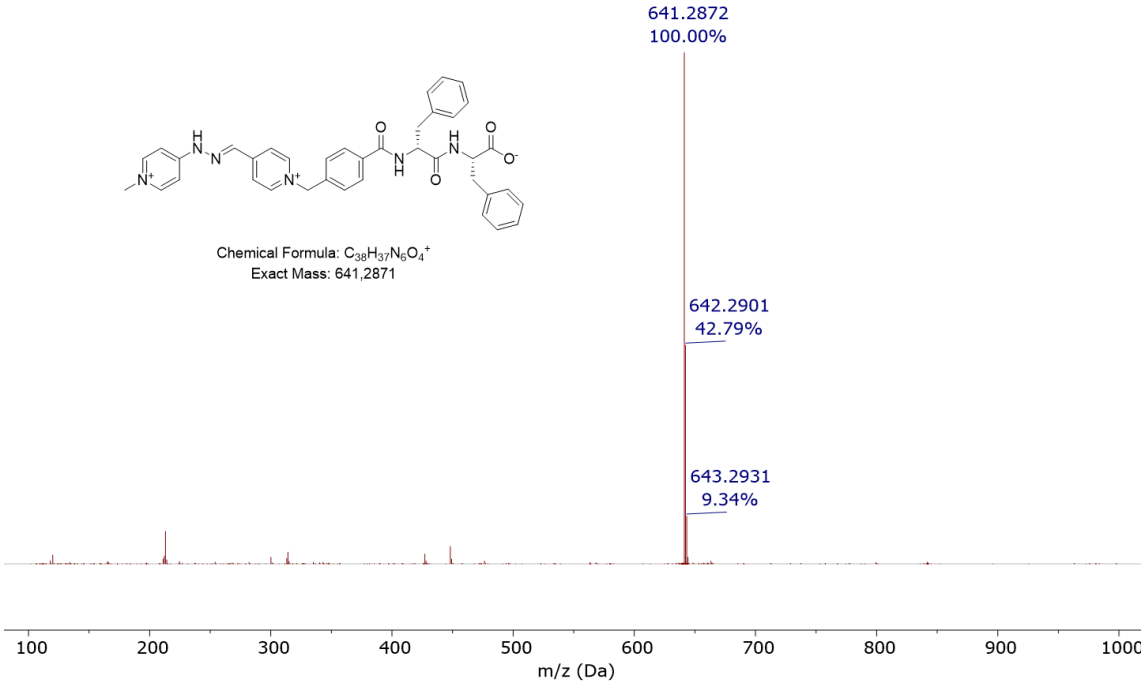

Fig. S22. ESI-HRMS spectrum of **V-fFH$_2$·2TFA**.

Spectroscopic data for V-FfFH$_2$·2TFA:

^{1}H NMR (500 MHz, DMSO-d6) δ 13.06 (br, 1H), 12.89 (br, 1H), 9.16 (d, *J* = 7.0 Hz, 2H), 8.59 (br, 2H), 8.56 (d, *J* = 8.5 Hz, 1H), 8.53 (d, *J* = 7.0 Hz, 2H), 8.50 (d, *J* = 8.6 Hz, 1H), 8.39 (d, *J* = 8.8 Hz, 1H), 8.33 (s, 1H), 8.00 (br, 1H), 7.80 (d, *J* = 8.4 Hz, 2H), 7.53 (d, *J* = 8.5 Hz, 2H), 7.30 – 7.01 (m, 16H), 5.85 (s, 2H), 4.65 (dddd, *J* = 14.8, 10.4, 8.7, 3.8 Hz, 2H), 4.49 (ddd, *J* = 10.3, 8.4, 4.5 Hz, 1H), 4.08 (s, 3H), 3.13 (dd, *J* = 13.7, 4.5 Hz, 1H), 2.84 (dd, *J* = 13.7, 10.2 Hz, 1H), 2.72 (dd, *J* = 13.3, 3.4 Hz, 1H), 2.65 (dd, *J* = 13.6, 3.6 Hz, 1H), 2.57 (dd, *J* = 13.2, 11.2 Hz, 1H), 2.45 (dd, *J* = 13.5, 10.2 Hz, 1H). **^{13}C NMR** (126 MHz, DMSO-d6) δ 172.86(CO_2H), 170.87 (C=O), 170.77(C=O), 165.17 (C=O), 153.64 (C_{Py}), 149.33 (C_{Py}), 145.49 (CH_{Py}), 145.04 (CH_{Py}), 140.83 (CH=N), 138.33 (C_{Ph}), 137.54 (C_{Ph}), 137.43 (C_{Ph}), 137.35 (C_{Ph}), 134.52 (C_{Ph}), 129.31 (CH_{Ph}), 129.28 (CH_{Ph}), 129.09 (CH_{Ph}), 128.27 (CH_{Ph}), 128.13 (CH_{Ph}), 128.06 (CH_{Ph}), 127.88 (CH_{Ph}), 127.79 (CH_{Ph}), 126.48 (CH_{Ph}), 126.17 (CH_{Ph}), 126.07 (CH_{Ph}), 124.93 (CH_{Ph}), 110.26 (CH_{Py}), 108.63 (CH_{Py}), 62.28 (CH_2), 54.77 (CH), 53.36 (CH), 53.33 (CH), 45.43 (CH_3), 38.23 (CH_2), 37.15 (CH_2), 37.14 (CH_2) ppm. **HR-MS (ESI)** (*m*/*z*): calcd for $[M]^+$ = 788.3555, found 788.3571.

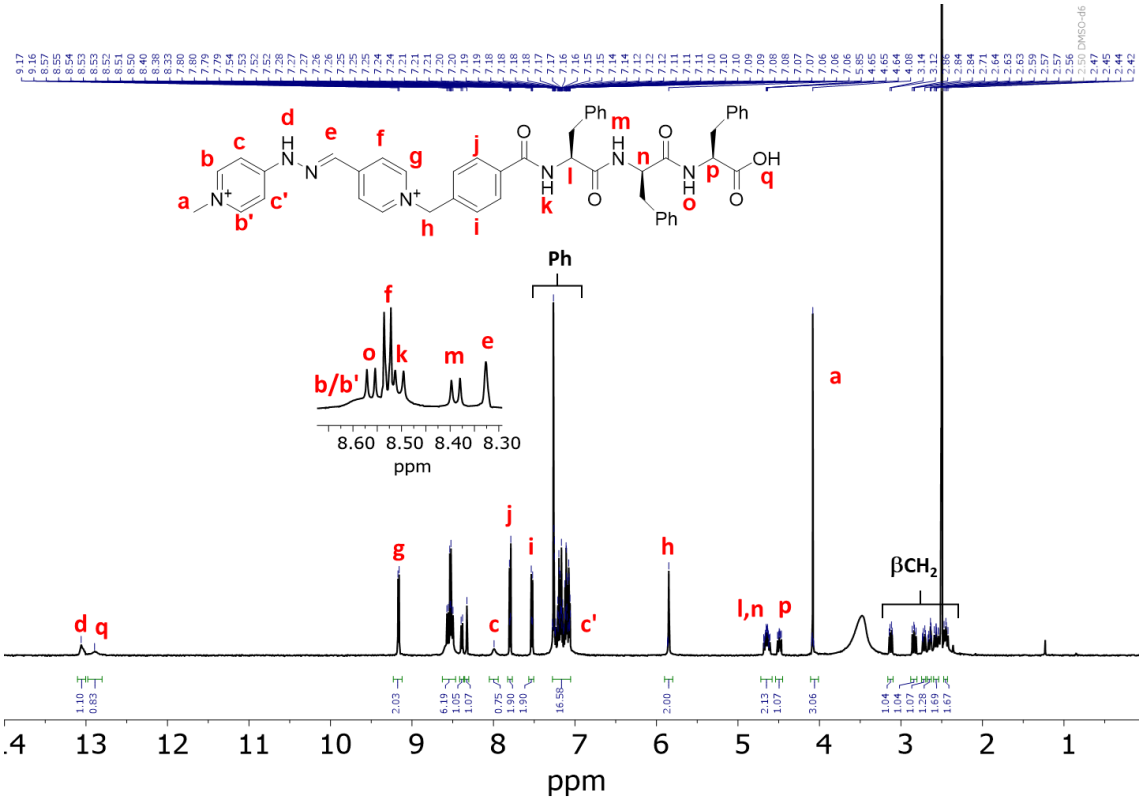

Fig. S23. ^{1}H-NMR (500 MHz, DMSO-d6) spectrum of **V-FfFH$_2$·2TFA**.

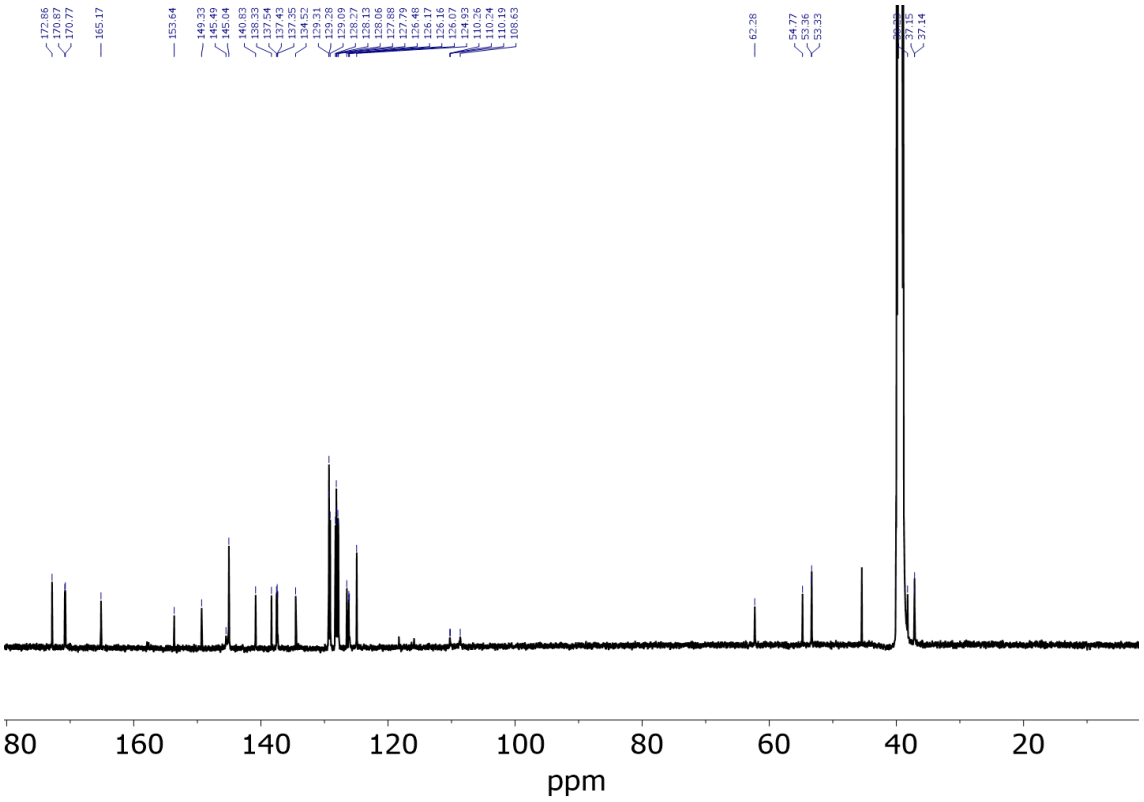

Fig. S24. ^{13}C-NMR (126 MHz, DMSO-d6) spectrum of **V-FfFH$_2$·2TFA**.

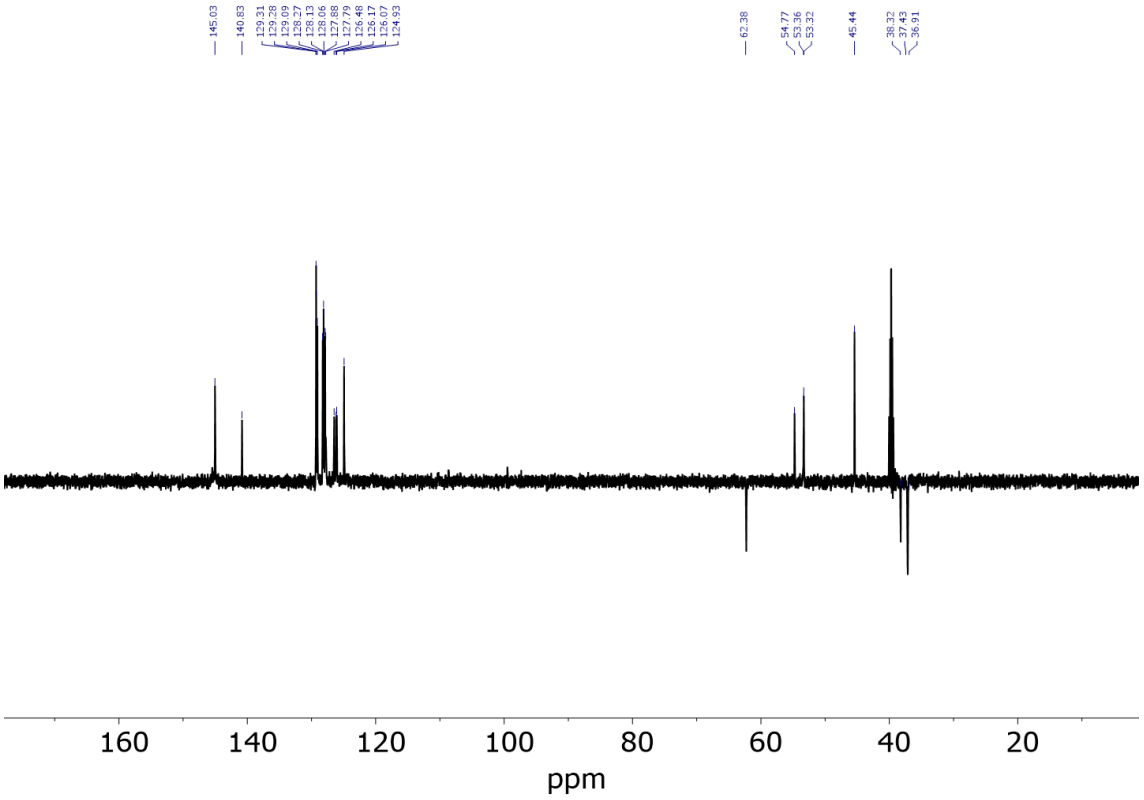

Fig. S25. DEPT-135 (126 MHz, DMSO-d6) spectrum of **V-FfFH$_2$·2TFA**.

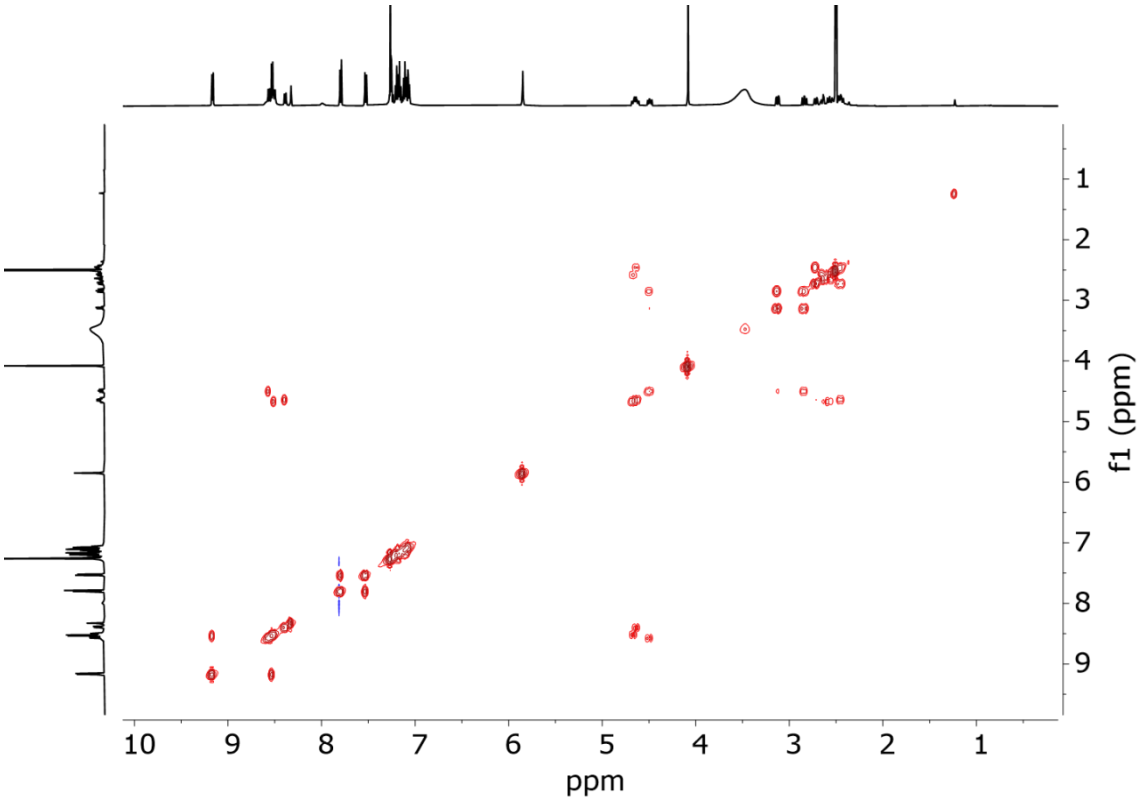

Fig. S26. ^{1}H-^{1}H COSY (500 MHz, DMSO-d6) spectrum of **V-FfFH$_2$·2TFA**.

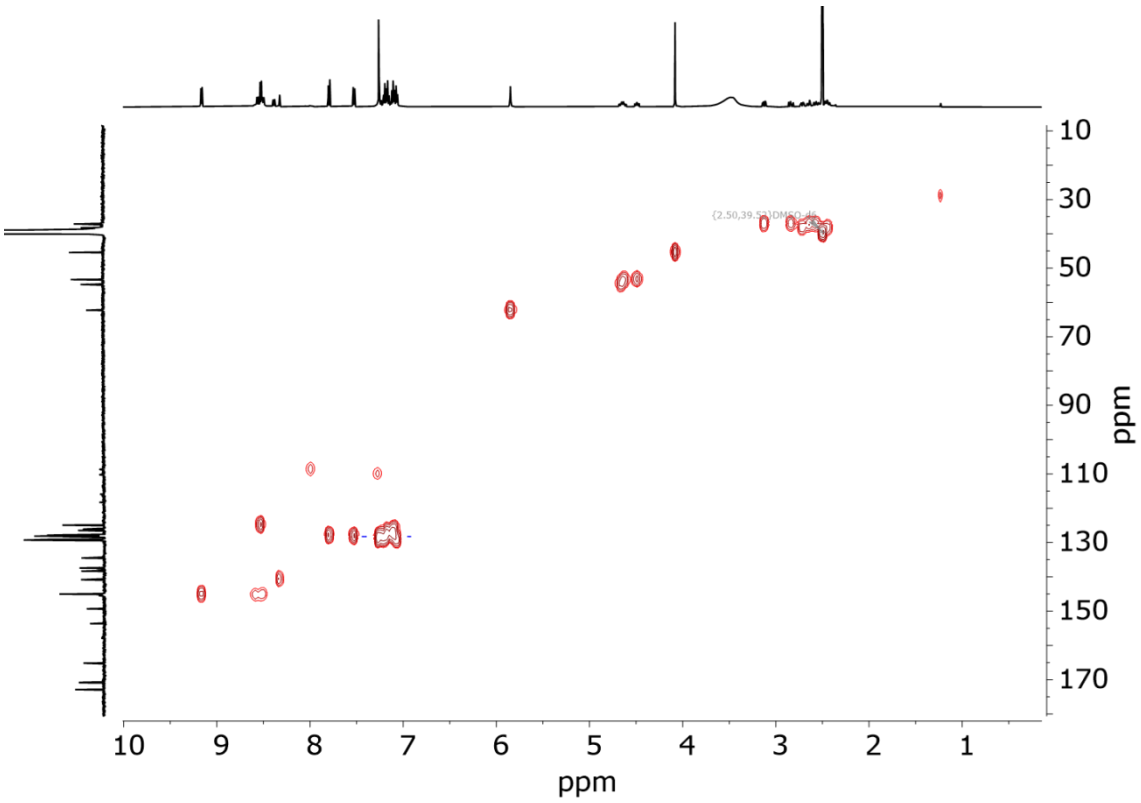

Fig. S27. ^{1}H-^{13}C HSQC (500 and 126 MHz, DMSO-d6) spectrum of **V-FfFH$_2$·2TFA**.

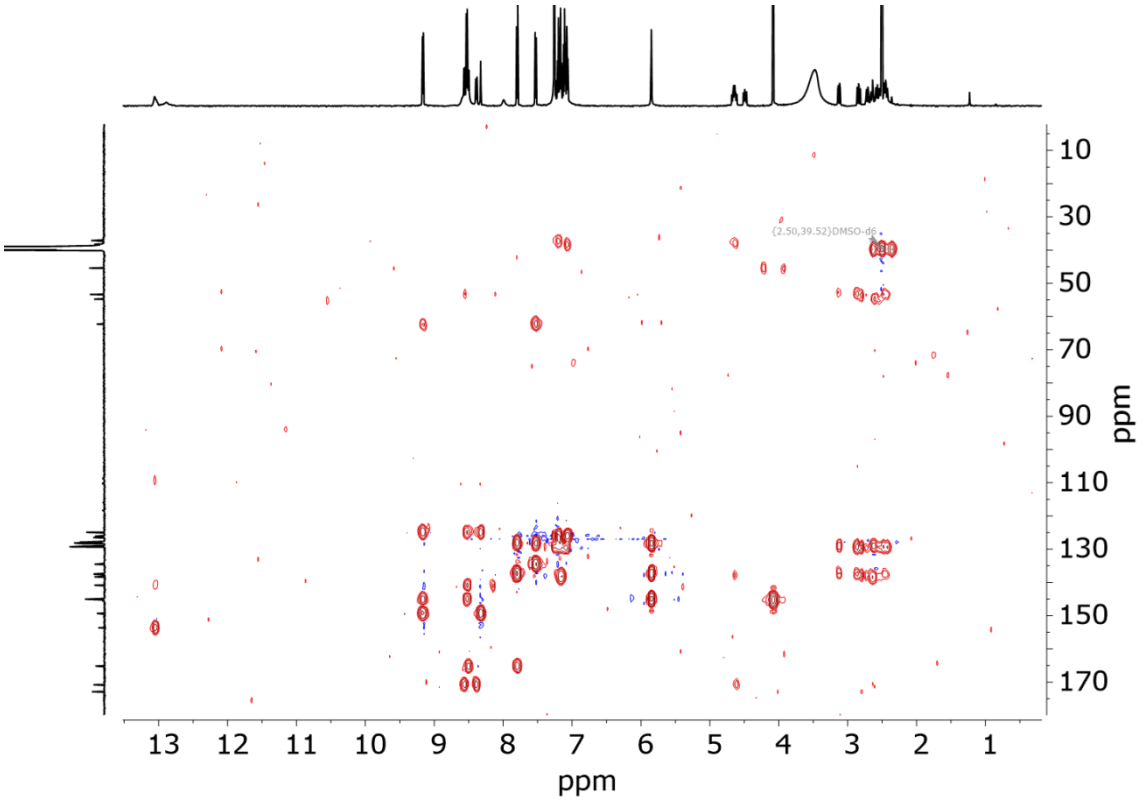

Fig. S28. ^{1}H-^{13}C HMBC (500 and 126 MHz, DMSO-d6) spectrum of **V-FfFH$_2$·2TFA**.

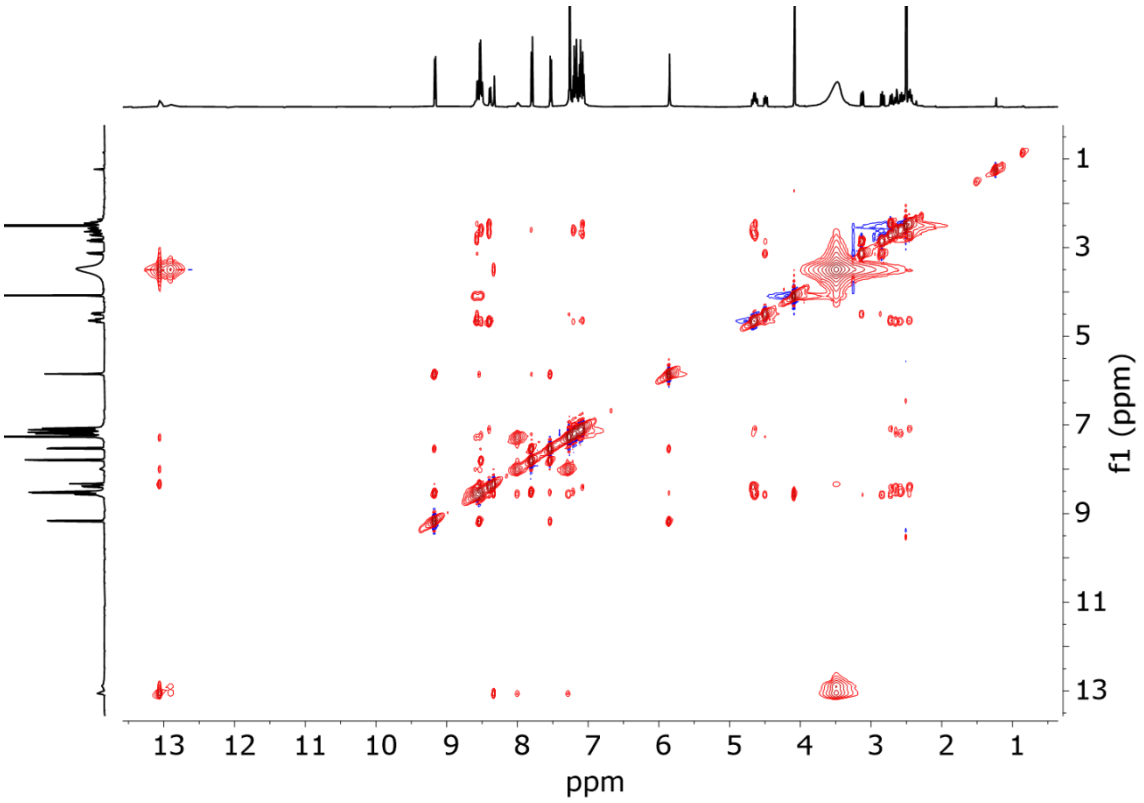

Fig. S29. ^{1}H-^{1}H NOESY (500 MHz, DMSO-d6) spectrum of **V-FfFH$_2$·2TFA**.

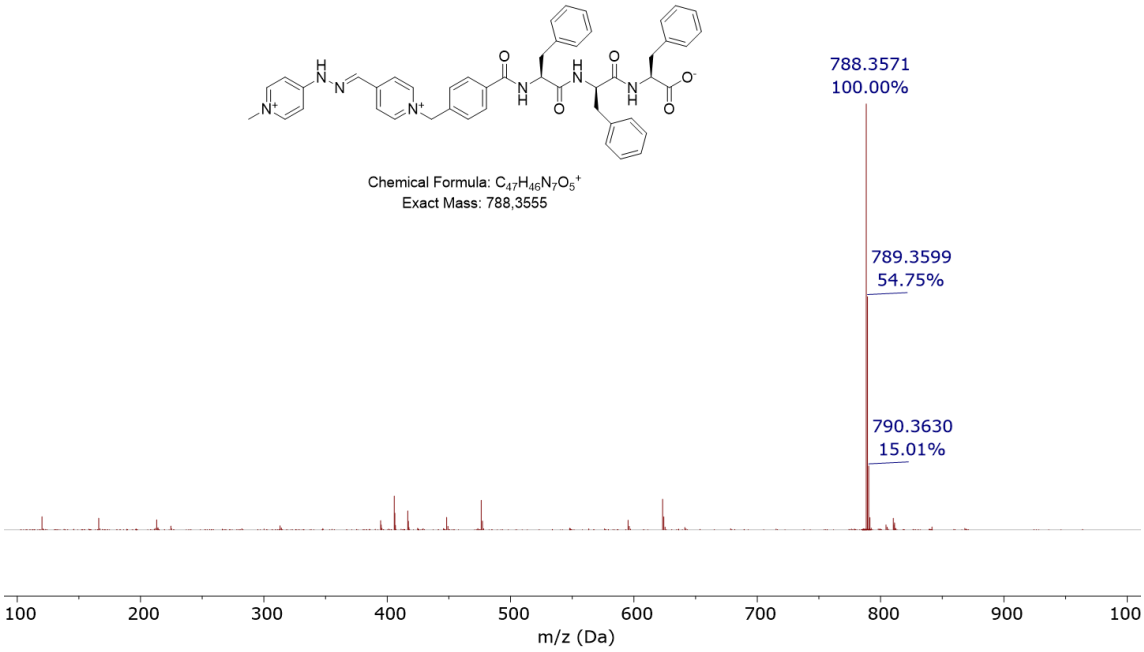

Fig. S30. ESI-HRMS spectrum of **V-FfFH$_2$·2TFA**.

S5. Ion metathesis.

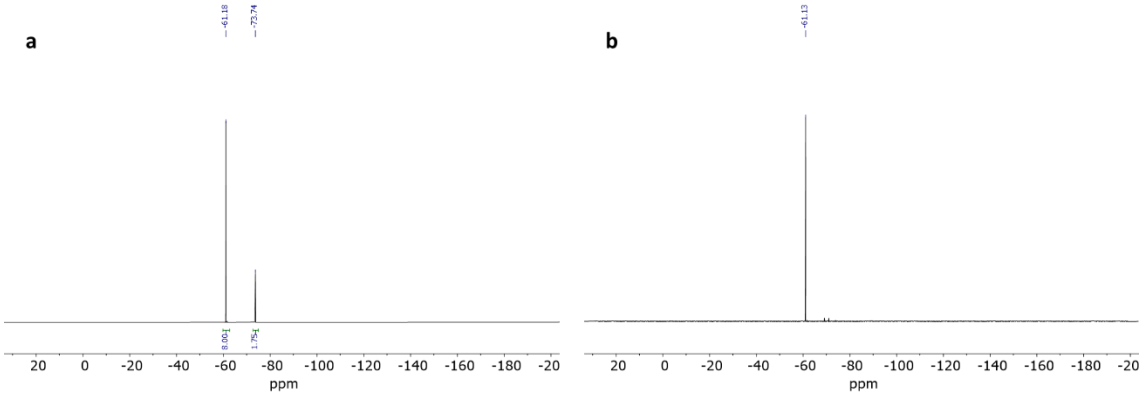

Fig. S31. ^{19}F-NMR (376 MHz, DMSO-d6) spectra of a) V-FfF·2TFA at 5.6 mM with an internal standard at 45 mM before metathesis, and b) V-FfF·2Cl at 6.6 mM with an internal standard at 53 mM after metathesis.

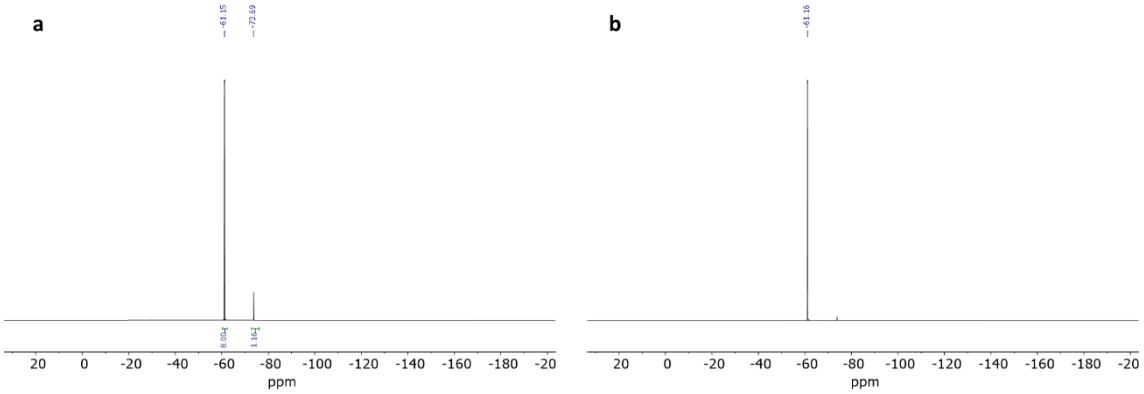

Fig. S32. ^{19}F-NMR (376 MHz, DMSO-d6) spectra of a) V-fF·2TFA at 6.6 mM with an internal standard at 53 mM before metathesis, and b) V-fF·2Cl at 8 mM with an internal standard at 64 mM after metathesis.

S6. pK_a determination.

Table S1. Experimental data obtained for the UV-vis titration of **V-FfF**H_2·2Cl at 20 µM in phosphate buffer (0.1M).

pH (measured)	ABS (479)	$\log[(A_{479}-A_{pH6.95})/(A_{pH10.92}-A_{479})]$
6,95	0,00679	-
7,5	0,02627	-1,62062
8	0,07701	-1,03573
8,5	0,2088	-0,49439
8,96	0,4019	-0,04427
9,54	0,65026	0,53176
10	0,76156	0,98661
10,92	0,8394	-

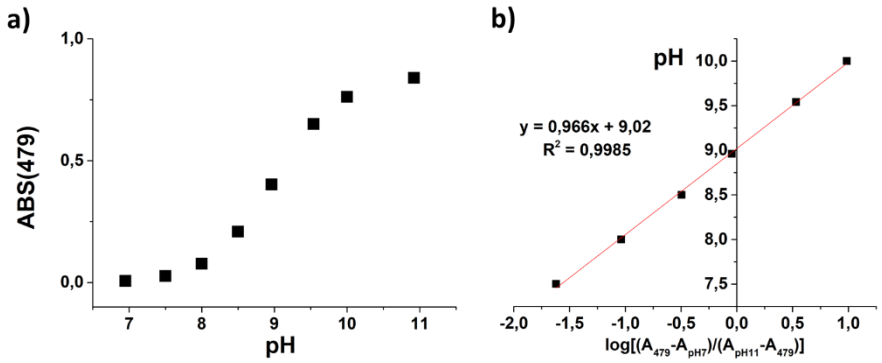

Fig. S33. a) Absorbance at 479 nm versus pH. b) Linear fitting of pH versus $\log[(A_{479}-A_{pH6.95})/(A_{pH10.92}-A_{479})]$, where p$K_a$ value is 9.02.

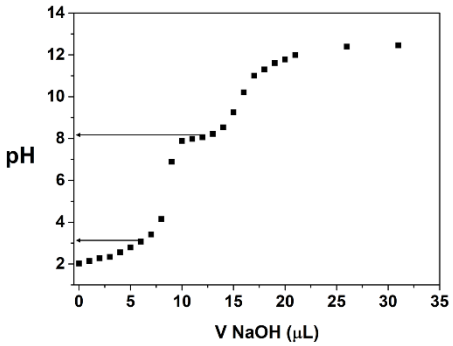

Fig. S34. pH titration for **V-f**H_2·2Cl at 10 mM.

S7. Rheology Characterization of hydrogels.

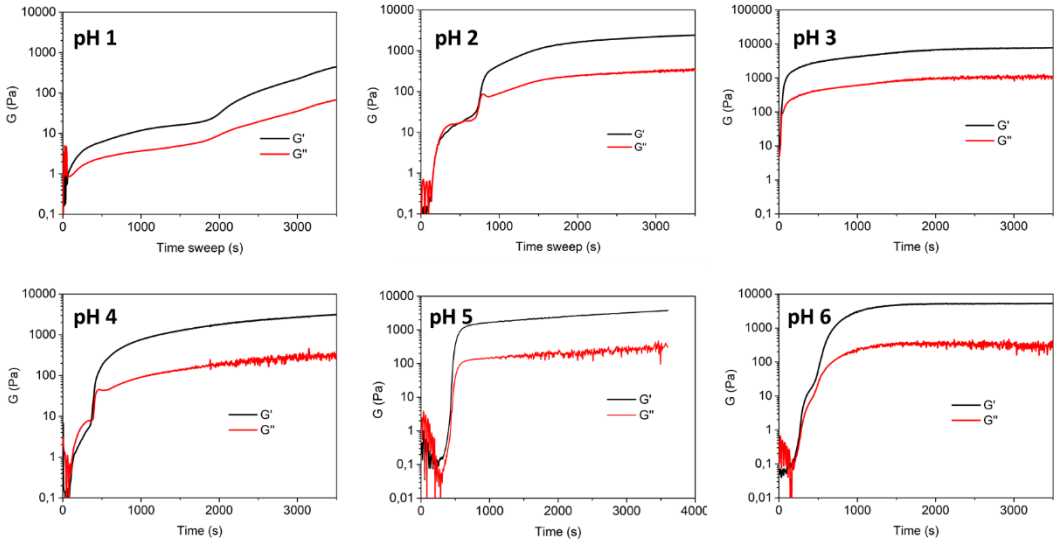

Fig. S35. Oscillatory rheology time sweeps experiments of **V-FfF**H_2·2Cl hydrogelation at different pH values.

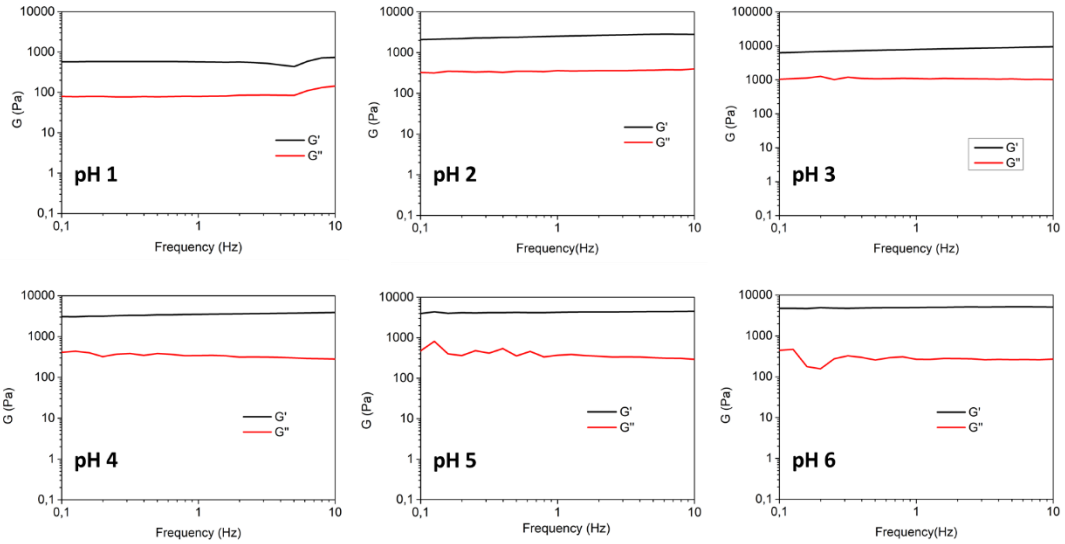

Fig. S36. Oscillatory rheology frequency sweeps experiments of **V-FfF**H_2·2Cl hydrogels at different pH values.

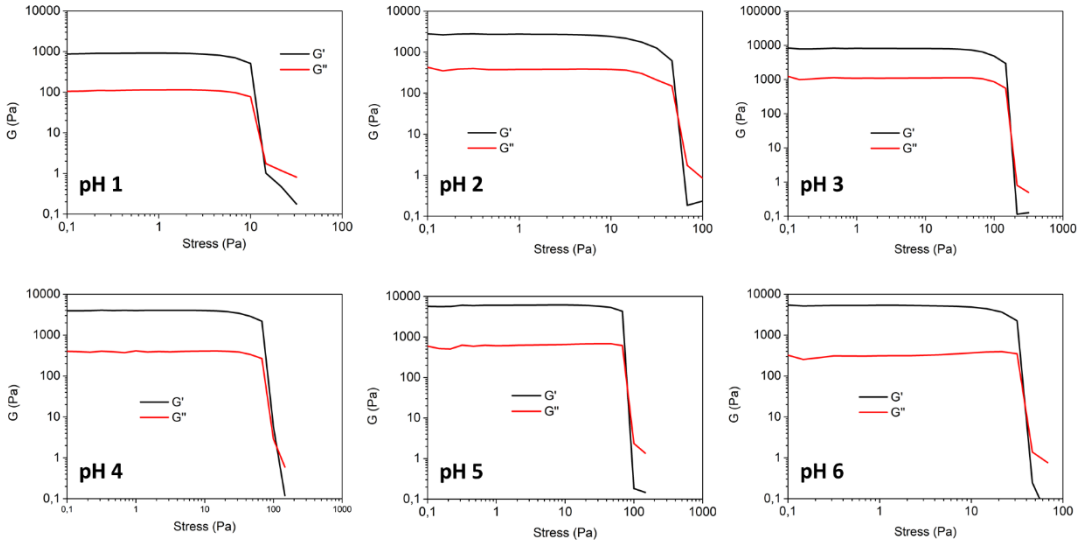

Fig. S37. Oscillatory rheology stress sweeps experiments of **V-FfF**H_2·2Cl hydrogels at different pH values.

S8. Thermoreversibility studies of hydrogels.

For the thermoreversion studies, hydrogels formed in the pH range 1–6 at a concentration of 10 mM V-FfFH$_2$·2Cl were used. The hydrogels were heated in a silicone oil thermostated bath at 100 °C until complete dissolution. Once fully dissolved, the sample was transferred to the rheometer and allowed to gel at 25 °C for 1 h. After this period, frequency sweep and stress sweep measurements were recorded.

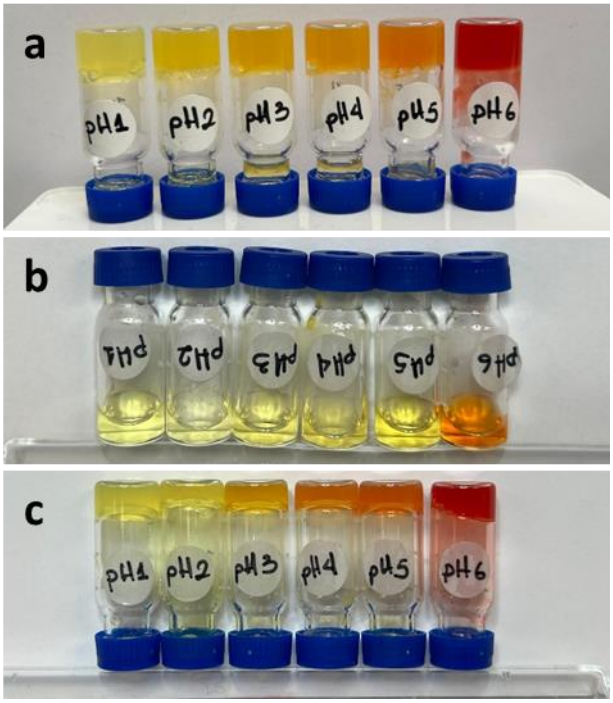

Fig. S38. a) Hydrogels prepared at different pH values before thermal treatment, b) samples fully dissolved after heating at 100 °C. c) Recovery of the gel state upon cooling to 25 °C, showing the thermoreversibility of **V-FfF**H$_2$·2Cl across the pH range.

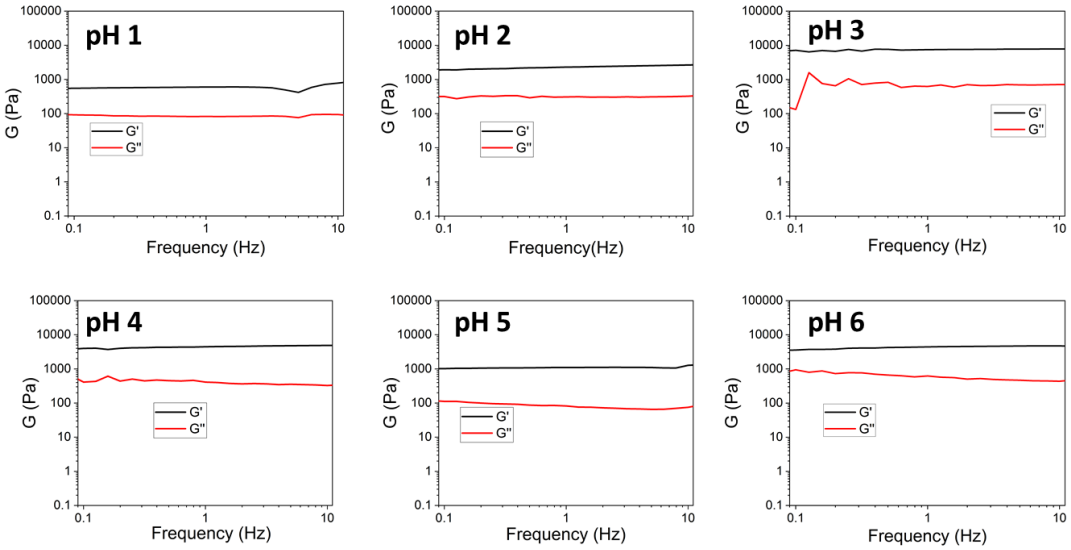

Fig. S39. Oscillatory rheology frequency sweeps experiments of **V-FfF**H$_2$·2Cl hydrogels at different pH values after thermal treatment.

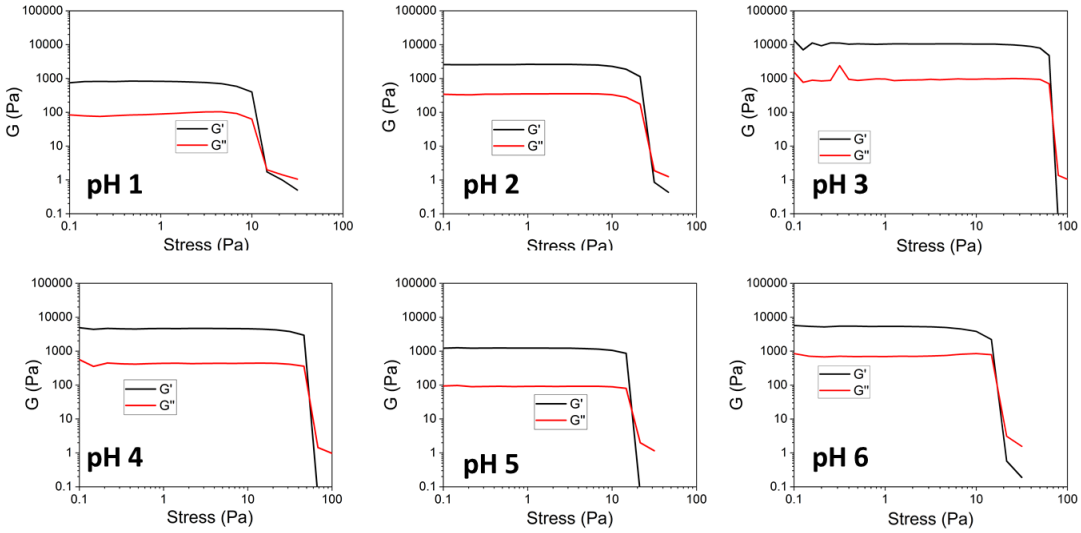

Fig. S40. Oscillatory rheology stress sweeps experiments of **V-FfF**H_2·2Cl hydrogels at different pH values after thermal treatment.

S9. TEM Analysis.

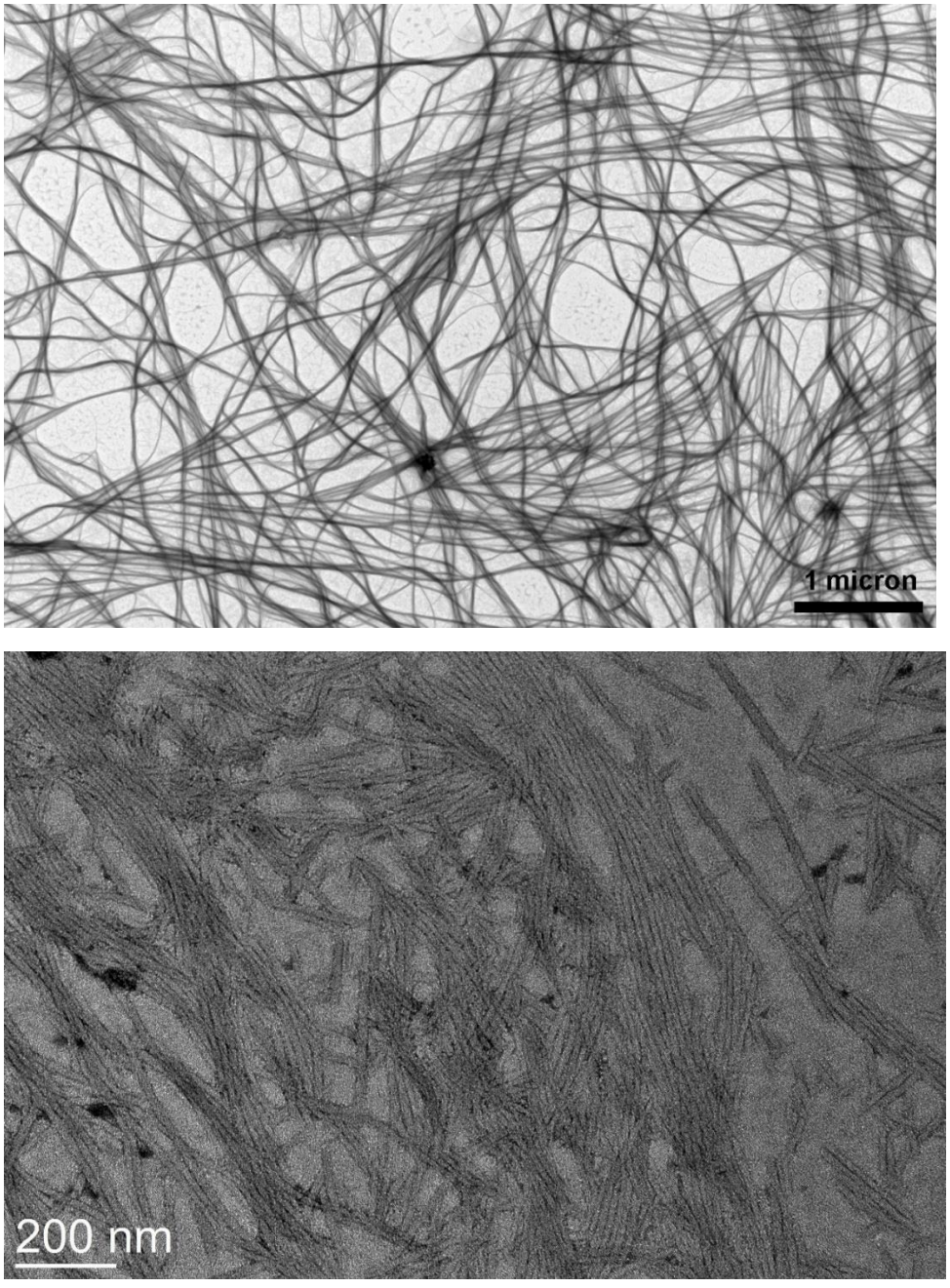

Fig. S41. TEM micrographs of the gelator at pH 1.

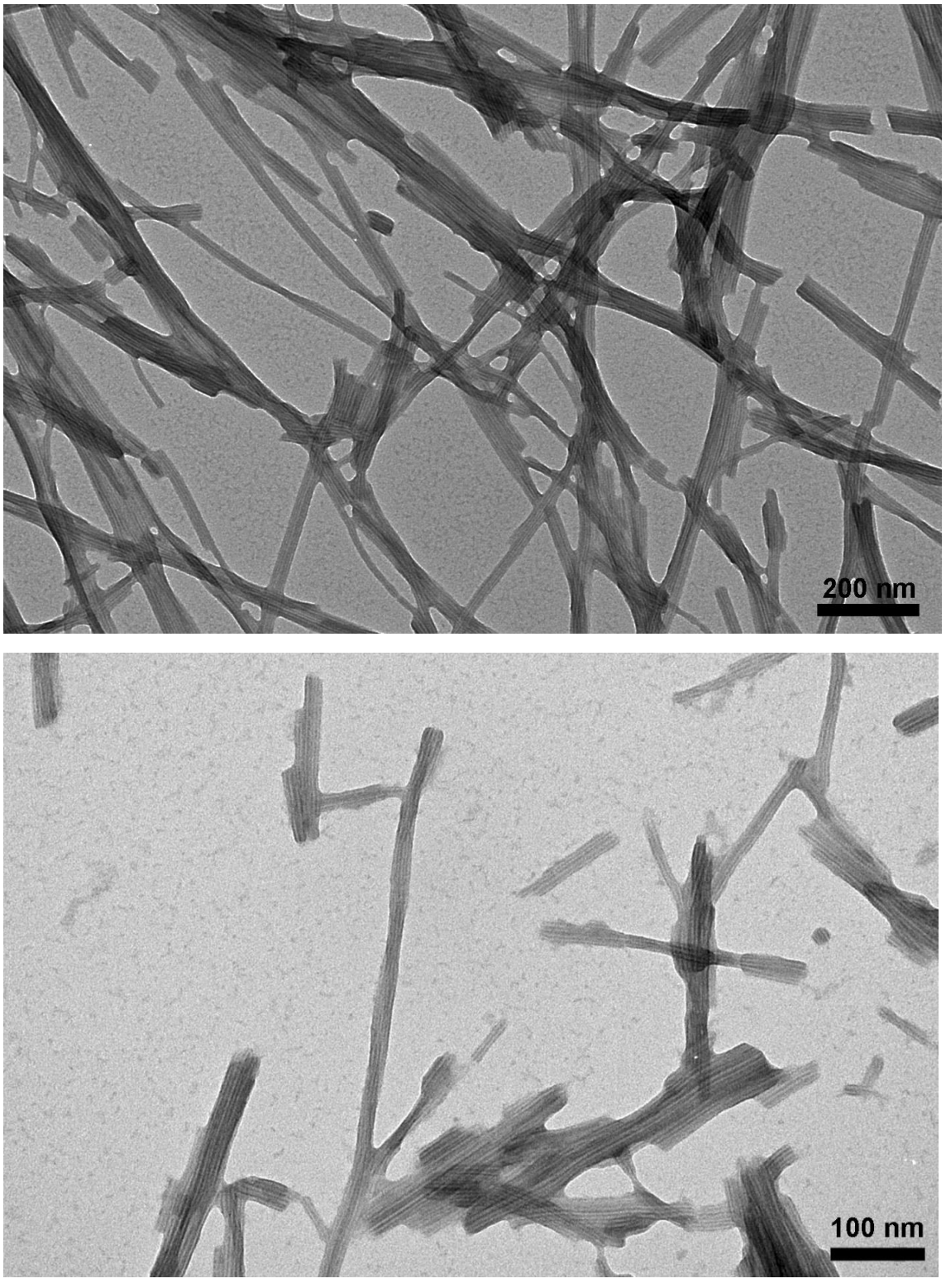

Fig. S42. TEM micrographs of the gelator at pH 2.

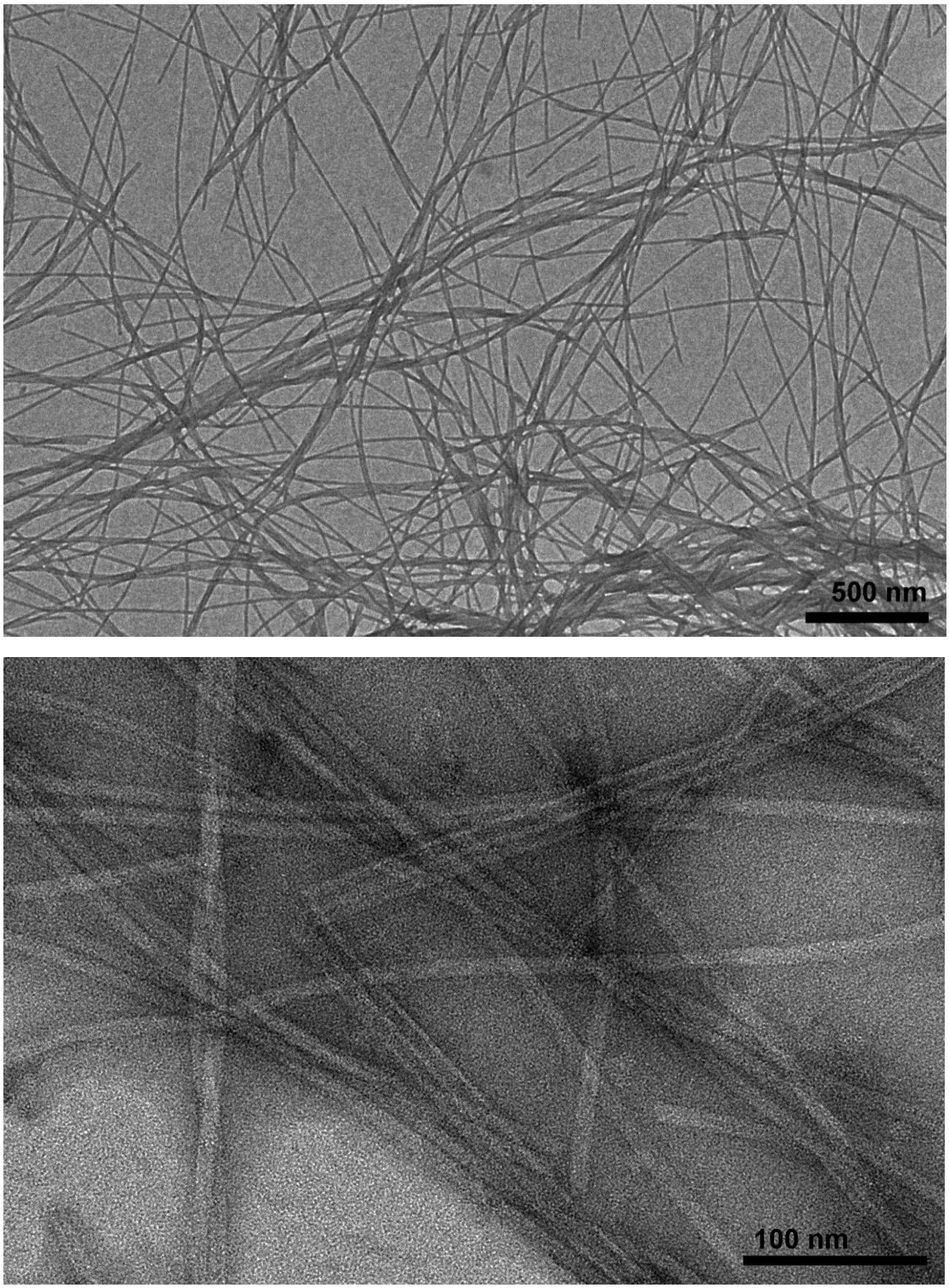

Fig. S43. TEM micrographs of the gelator at pH 3.

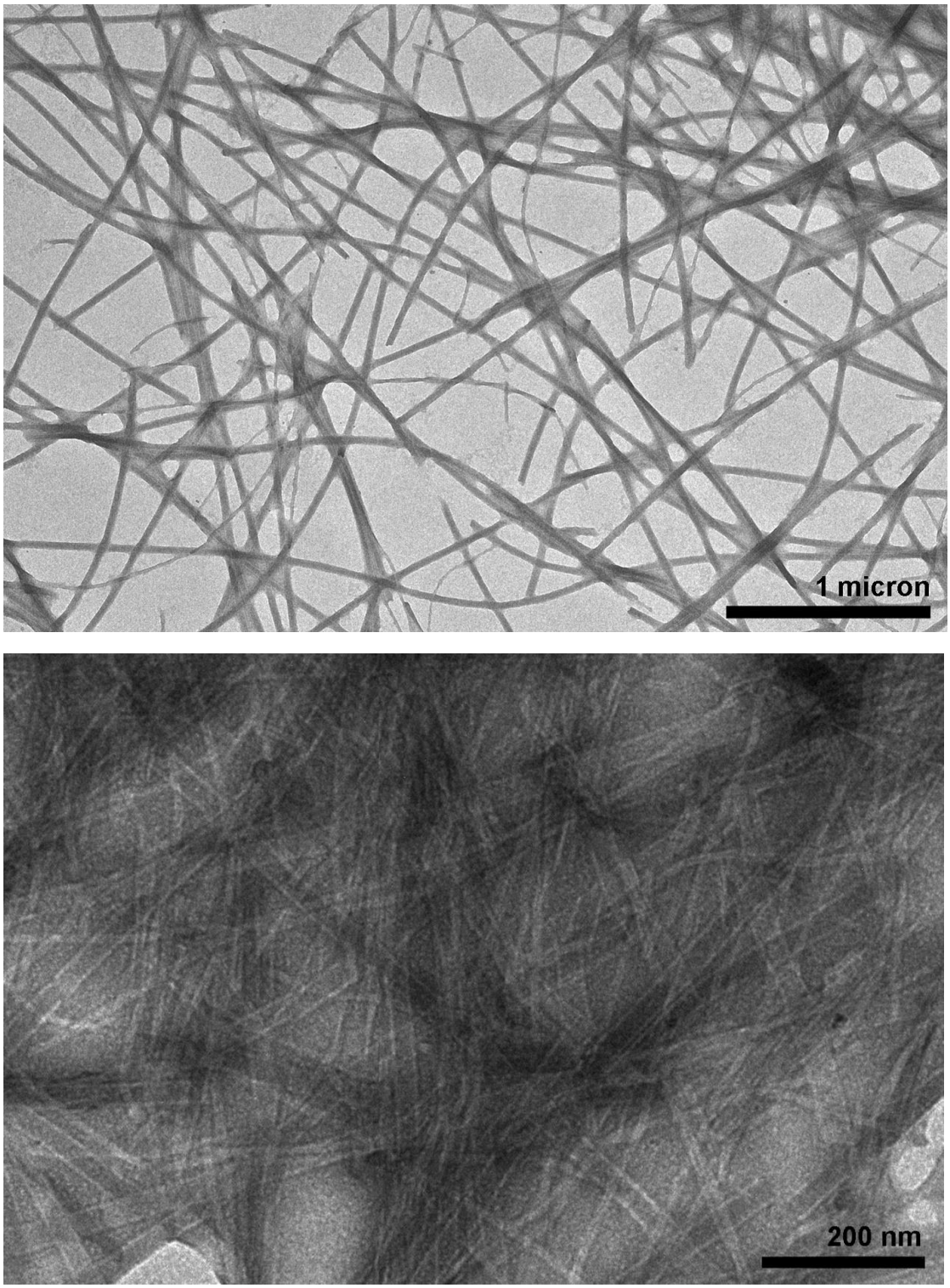

Fig. S44. TEM micrographs of the gelator at pH 4.

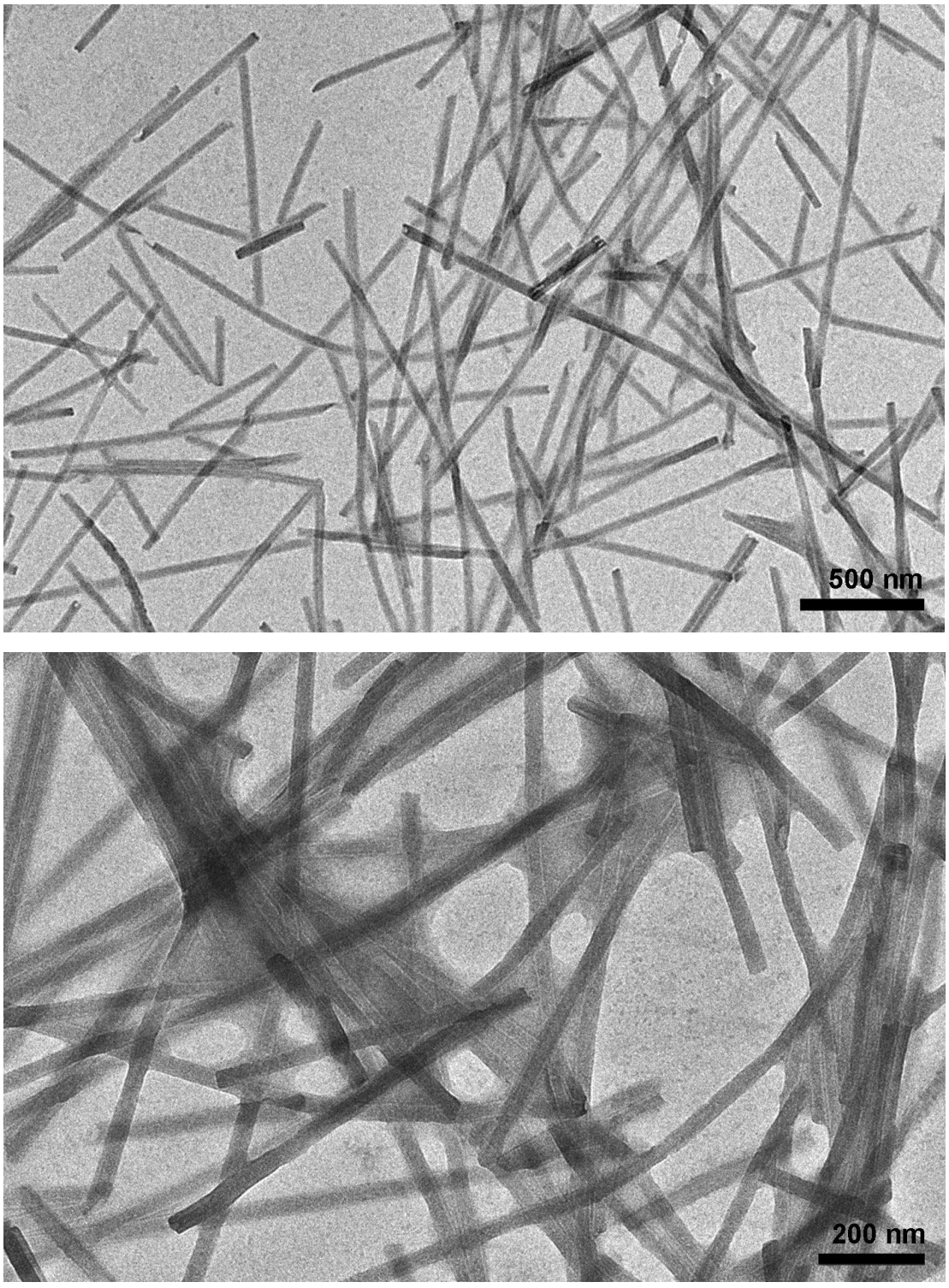

Fig. S45. TEM micrographs of the gelator at pH 5.

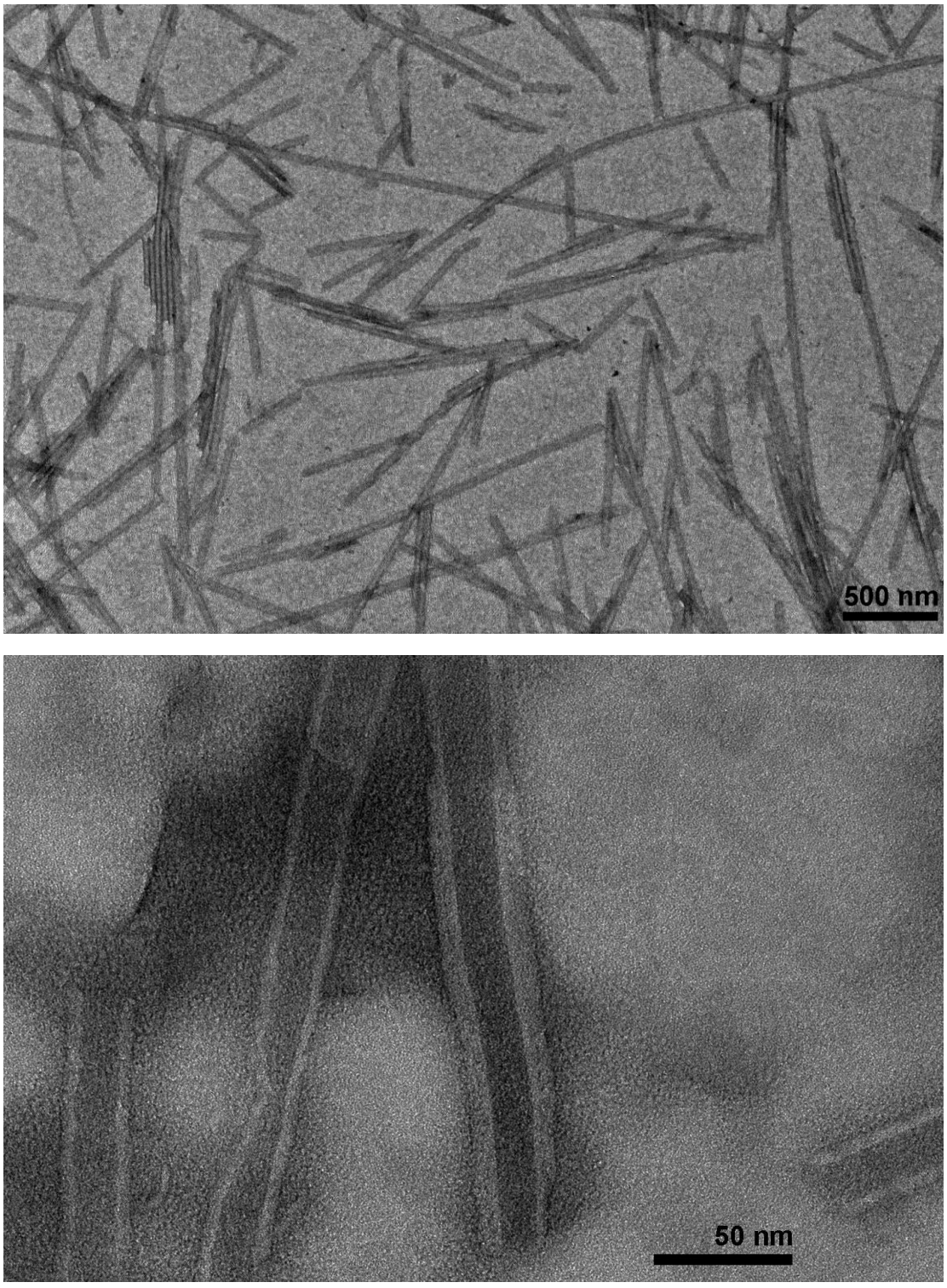

Fig. S46. TEM micrographs of the gelator at pH 6.

S10. SEM Analysis.

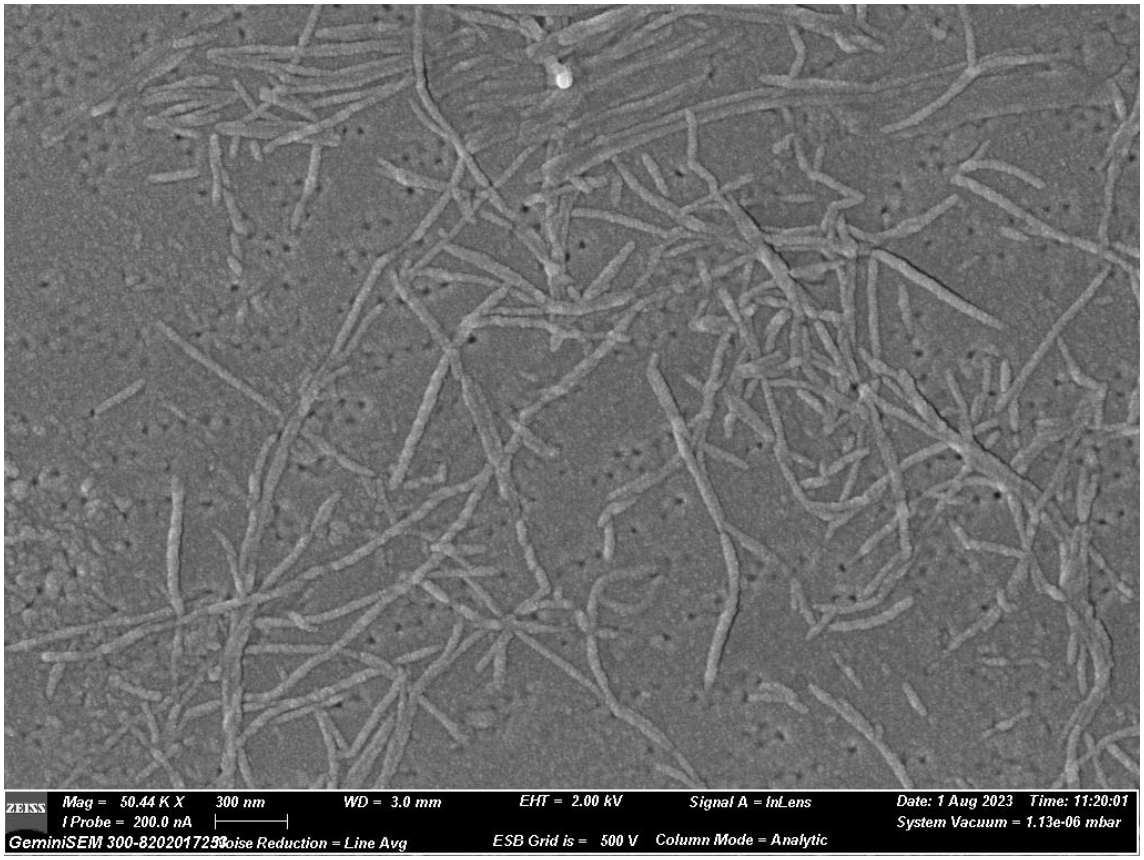

Fig. S47. SEM image of the gelator at pH 1.

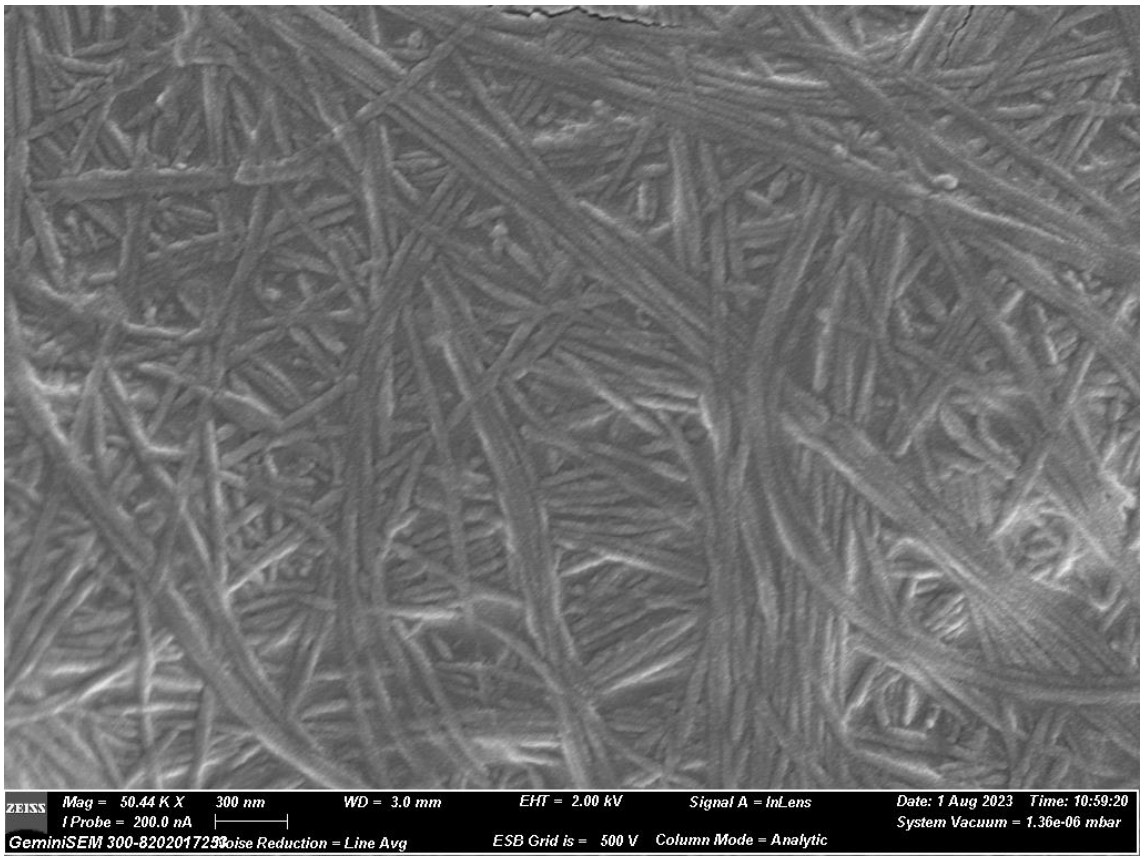

Fig. S48. SEM image of the gelator at pH 6.

S11. Assessment of morphological changes by pH in preformed hydrogel.

To assess the dynamic behavior associated with pH-driven nanostructural changes, a **V-FfF**H_2·2Cl hydrogel (8.6 mg/mL) previously formed at pH 1.5 was subjected to a pH increase to 6.2 by the addition of 1 M NaOH and monitoring the pH with a pH-meter (**Fig. S49**). TEM analysis of the hydrogel at pH 1.5 (**Fig. S50**) and after basification (**Fig. S51**) reveals a clear structural transition from nanofibers to nanotubes.

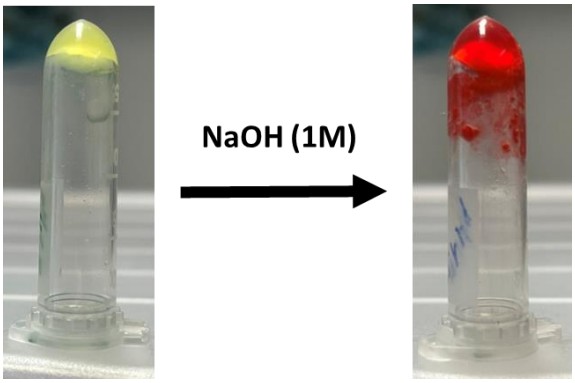

Fig. S49. Images of the hydrogel prepared at pH 1.5 (left panel), and the same hydrogel after basification until pH 6.2 with NaOH solution (right panel).

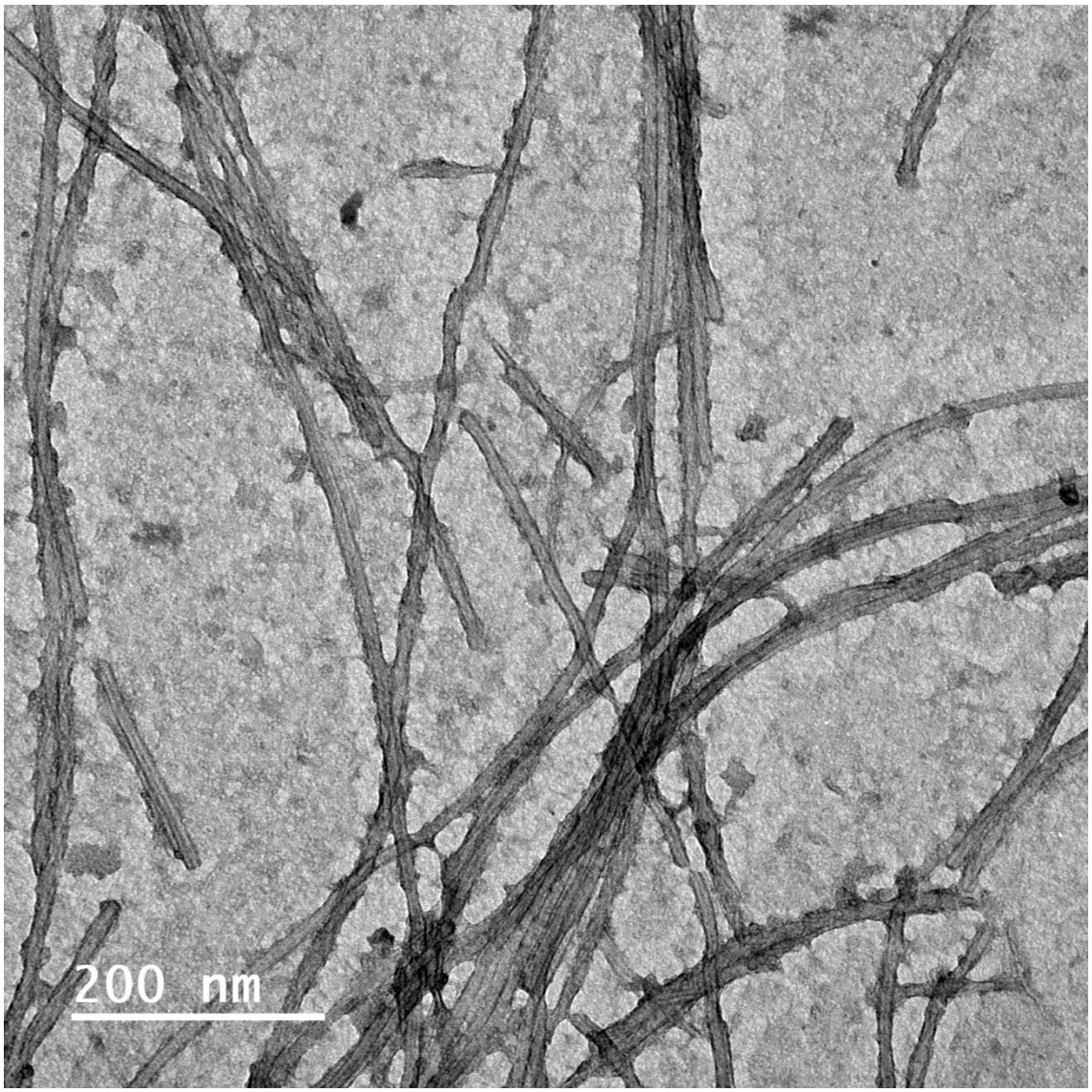

Fig. S50. TEM micrographs of the gelator at pH 1.5 before basification.

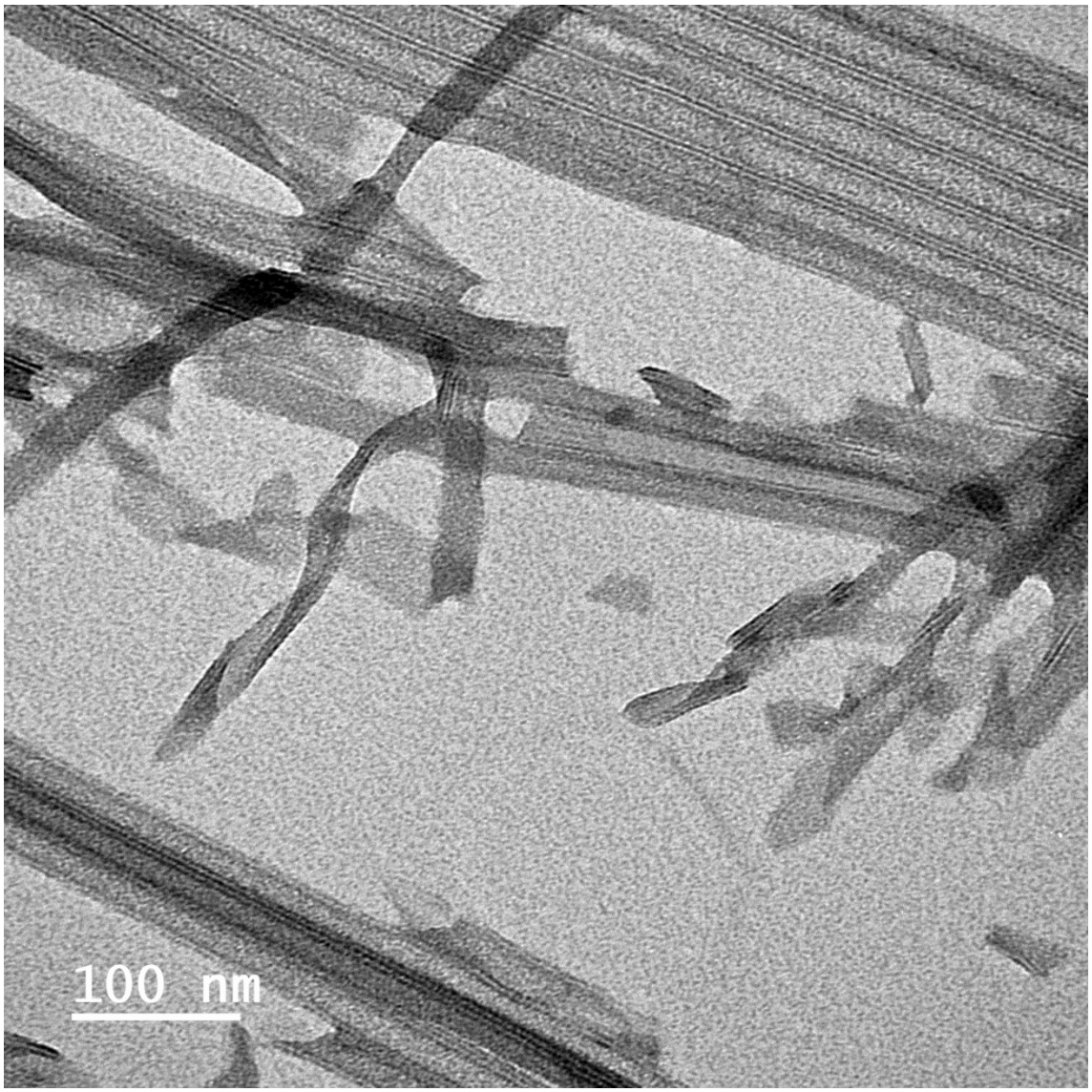

Fig. S51. TEM micrographs of the gelator at pH 6.2 after basification with 1M NaOH solution.

S12. Single-crystal XRD data (CCDC2420787)

The pseudopeptide crystallized in the triclinic crystal system with the space group *P1*. The asymmetric unit is composed by two independent pseudopeptide molecules, a methanol molecule with an occupancy of 0.7, and two water molecules. The compound is zwitterionic and no counterions were detected. Disordered water molecules are present in the cavity between the hydrazone moieties. Their electron density was interpreted and refined by SQUEEZE (PLATON).[2] The compound packed in alternate hydrophobic and hydrophilic layers (**Fig. S46**). The hydrophobic layers are composed by the three phenylalanine rings whereas the hydrazone moiety is packed in the hydrophilic region of the structure. Two different hydrophilic cavities are present in the layer: the first one accommodates two water molecules which bridge via hydrogen bonding the C-terminal carboxylates and the hydrazone (Error! Reference source not found. **S47**), the second one is composed by disordered water molecules and a molecule of methanol.

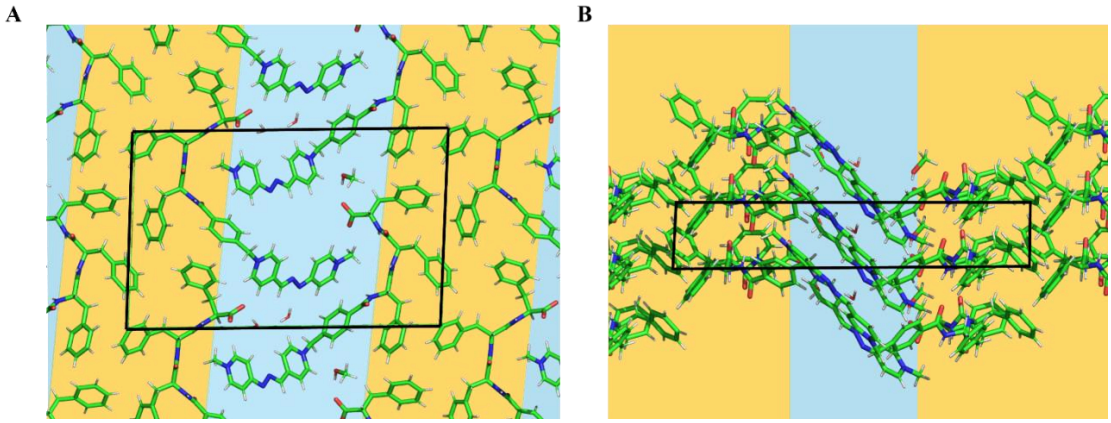

Fig. S52. V-FfF unit cell. A) view along the a crystallographic axis B) view along the b crystallographic axis. The peptide packed in alternate hydrophobic (brown) and hydrophilic (light blue) layers. The hydrophobic layer is composed by the segregation of the three phenylalanine side chains whereas the hydrophilic by the hydrazone moiety and the C-terminal carboxylate. The compound is represented in stick model. Green: carbon, red: oxygen, blue: nitrogen, white: hydrogen.

[2] Spek, A. L. PLATON SQUEEZE: A Tool for the Calculation of the Disordered Solvent Contribution to the Calculated Structure Factors. *Acta Crystallogr. Sect. C Struct. Chem.* **2015**, *71*, 9–18.

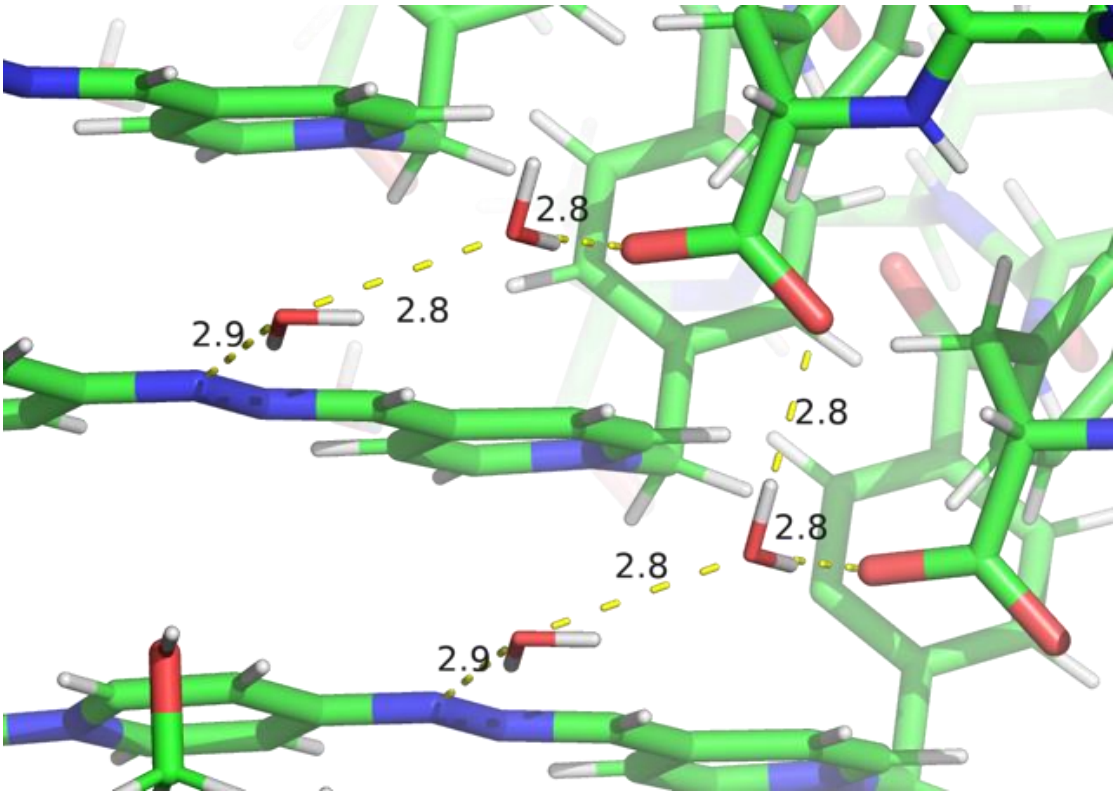

Fig. S53. Hydrogen bond network between carboxylates and the hydrazone in the smallest hydrophilic cavity.

The two independent conformers display different orientation of the hydrazone moiety (**Fig. S48A**) due to the different ϕ torsional angle of the Phe 1 residue (green -123.5°, cyan -134.5). The extended π-conjugation of the two pyridinium rings and the deprotonated hydrazone flattened this moiety in a rigid body which changed significantly in position with the ~10° rotation of the ϕ angle. The peptide backbone interacts via hydrogen bonding through the amide groups in a parallel β-sheet motif (**Fig. S48B**).

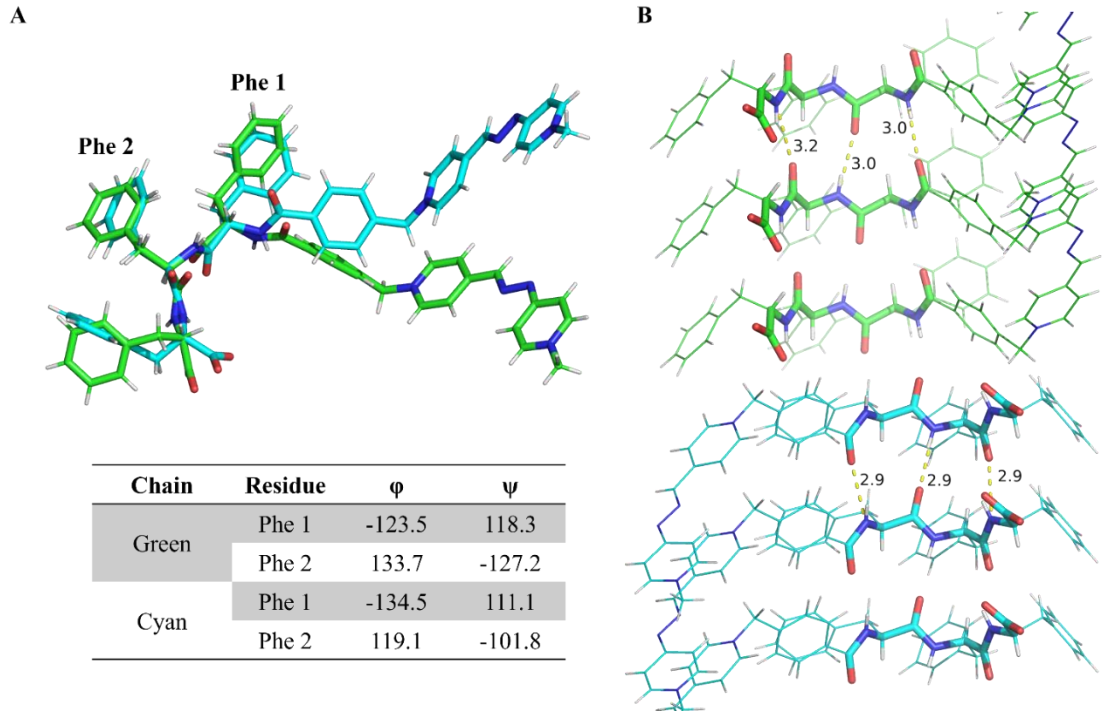

Chain	Residue	φ	ψ
Green	Phe 1	-123.5	118.3
	Phe 2	133.7	-127.2
Cyan	Phe 1	-134.5	111.1
	Phe 2	119.1	-101.8

Fig. S54. A) Superimposition of the two independent pseudopeptide molecules and Phe dihedral angles. B) Hydrogen bond network between amide groups of the backbone.

The compound crystallised as zwitterion and the two terminal groups form salt bridges in a head-to-tail fashion (**Fig. S49**). The C-terminal carboxylate of the green molecule forms the hydrogen bond network described in **Fig. S47** and the distance between the pyridinium aromatic ring suggested an ionic interaction between them.

The carboxylate group of the cyan molecule interacts as well with a pyridinium ring and probably with the disordered water inside the cavity. The hydrogen bond network described in **Fig. S47** highlights a water bridge between the deprotonated hydrazone and the carboxylate of another green molecule. It is possible that this kind of water bridge is present also between cyan molecules. The methanol molecule act as a donor in a hydrogen bond interaction with the carboxylic group of the cyan molecule.

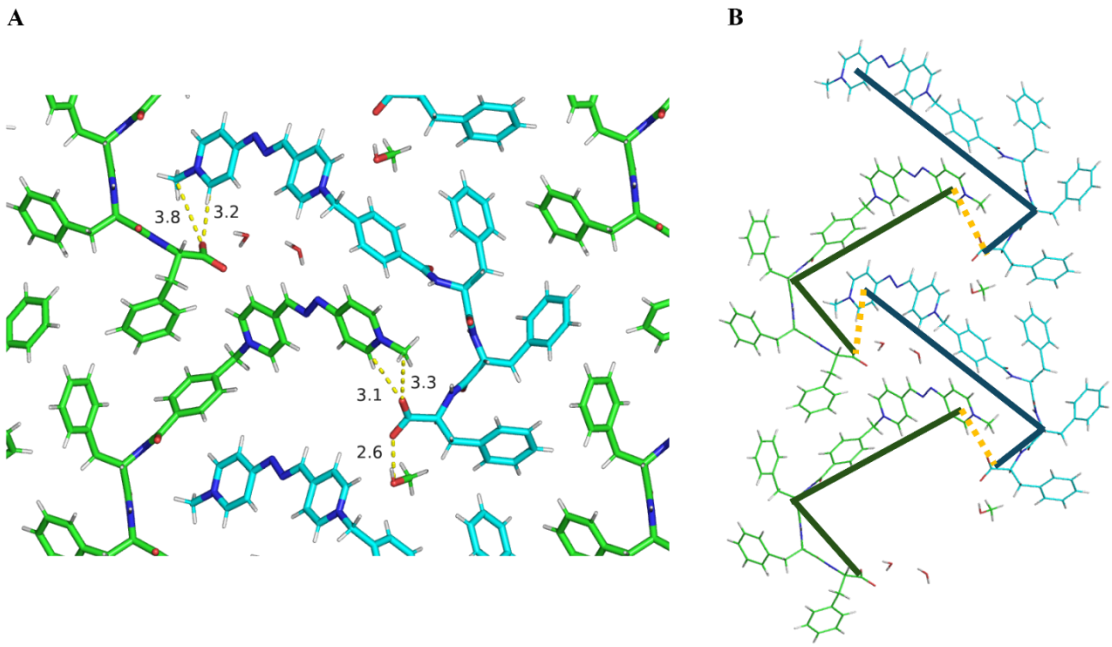

Fig. S55. A) Salt bridges between the C-terminal carboxylate and the N-methyl pyridinium moiety. B) The peptide crystallised as zwitterion in head-to-tail fashion.

Experimental details.

The compound was dissolved in methanol and then diluted with water in a 50/50 final ratio. A small amount of sodium hydroxide solution was added to rise the pH value around 6. The solution turned from yellow to red and gel aggregates formed. After one month, the gel aggregates evolved in red crystals.

Single crystals were loaded on cry-loops and cryoprotected in NHV oil (Jena bioscience, Germany). The crystals were loaded on the goniometer and cooled down at 100 K (XRD1 beamline, Elettra synchrotron). The data collection was performed on 5 different samples by XDS,[3] space groups were assigned by POINTLESS[4] and the two best results were merged by XSCALE[5] to reach the final completeness of 99.1%. The phase problem was solved by direct methods by XPREP and SHELXT.[6] The model was refined by SHELXL[7] using the SHELXLe GUI.[8] The disordered solvent was refined by PLATON SQUEEZE. The model was then validated by PLATON[9] and the final CIF was compiled by WINGX GUI.[10]

[3] Kabsch, W. XDS. *Acta Crystallogr. D Biol. Crystallogr.* **2010**, *66*, 125–132.
[4] Evans, P. R. Scaling and Assessment of Data Quality. *Acta Crystallogr. D Biol. Crystallogr.* **2006**, *62*, 72–82.
[5] Kabsch, W. XSCALE. *Urnisbn978-0-470-66078-2* **2012**, *F*, 304–310.
[6] Sheldrick, G. M. SHELXT – Integrated Space-Group and Crystal-Structure Determination. *Acta Crystallogr. Sect. Found. Adv.* **2015**, *71*, 3–8.
[7] Sheldrick, G. M. Crystal Structure Refinement with SHELXL. *Acta Crystallogr. Sect. C Struct. Chem.* **2015**, *71*, 3–8.
[8] Hübschle, C. B.; Sheldrick, G. M.; Dittrich, B. ShelXle: A Qt Graphical User Interface for SHELXL. *J. Appl. Crystallogr.* **2011**, *44*, 1281–1284.
[9] Spek, A. L. Single-Crystal Structure Validation with the Program PLATON. *J. Appl. Crystallogr.* **2003**, *36*, 7–13.
[10] Farrugia, L. J. WinGX Suite for Small-Molecule Single-Crystal Crystallography. *J. Appl. Crystallogr.* **1999**, *32* (4), 837–838.

Crystallographic data.

	VM-FfF
Formula	$C_{47}H_{45}N_7O_5$, 0.7($C_1H_4O_1$), 2(H_2O)
Temperature (K)	100
Wavelength (Å)	0.7
Crystal system	Triclinic
Space group	*P 1*
a (Å)	4.9700(10)
b (Å)	16.570(3)
c (Å)	26.380(5))
α (°)	92.56(3)
β (°)	91.80(3)
γ (°)	97.83(3)
V ($Å^3$)	2148.5(8)
Z, ρcalc (g/cm^3)	2, 1.264
μ (mm^{-1})	0.082
F (000)	865
Data collection θ range	0.762- 25.942
Refl. Collected / unique	56489 / 17482
Rint	0.0831
Completeness (%)	99.1
Data/Restraints/Parameters	17482 / 9 / 1121
GooF	1.058
R1, wR2 [I>2σ(I)]	0.0525 / 0.1386
R1, wR2 all data	0.0637 / 0.1463

S13. ATR-IR Characterization.

A small portion of the hydrogel was deposited on a 1cm^2 silicon wafer 2 hours after gelation. The silicon wafer with the hydrogel was dried under vacuum for 24 hours. All spectra were acquired at resolution of 4 cm^{-1} and 120 scans on a Shimadzu QATR-10 (diamond crystal).

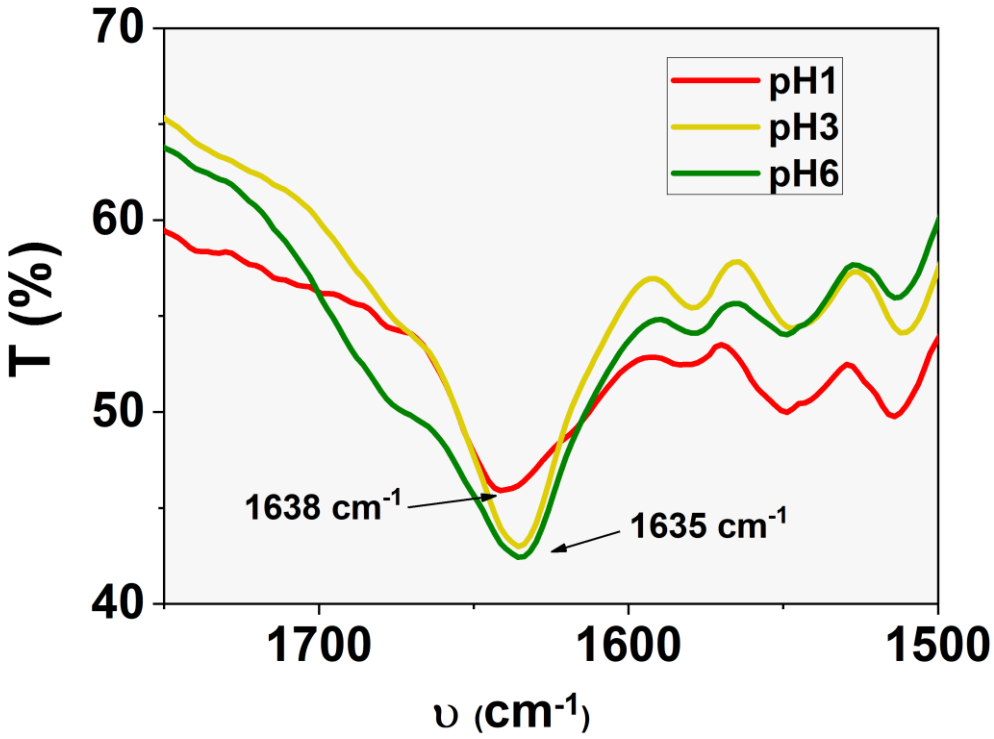

Fig. S56. Amide-I region of the IR spectra of the xerogels obtained at pH 1 and pH 6.

S14. Circular Dichroism (CD) Characterization.

CD spectra were recorder using a Jasco J-815 CD spectrophotometer with a Xenon lamp of 150 W. All samples were measured in a 0.1 mm quartz cell just after solubilizing **V-FfF**H_2·2Cl in its corresponding buffer. All measurements were carried out at a scan rate of 100 nm/min, 2 sec D.I.T., and a bandwidth of 2 nm.

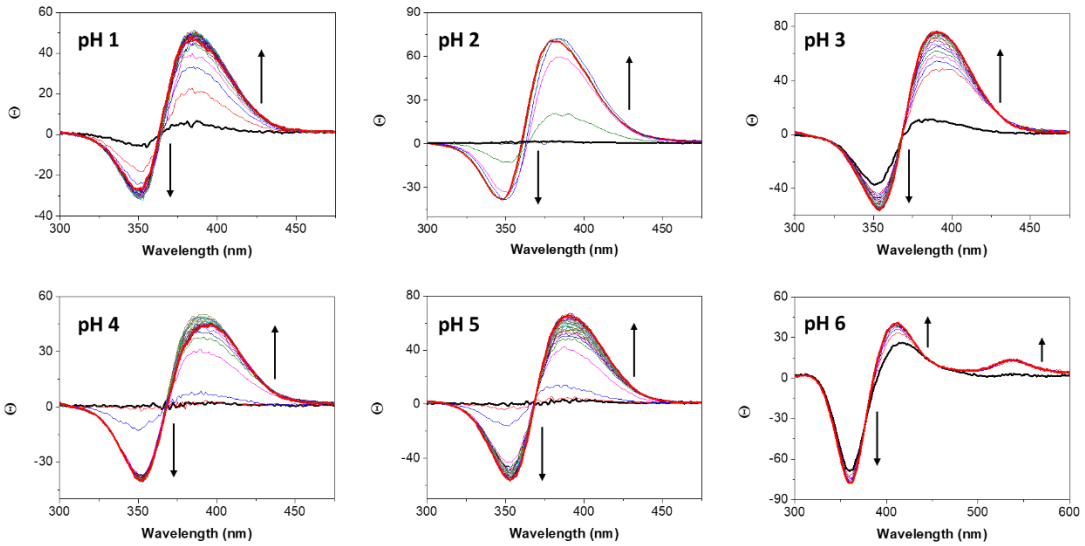

Fig. S57. Monitoring of hydrogel formation by CD over the course of 1 hour. All hydrogels were studied at 5 mM in their corresponding buffer.

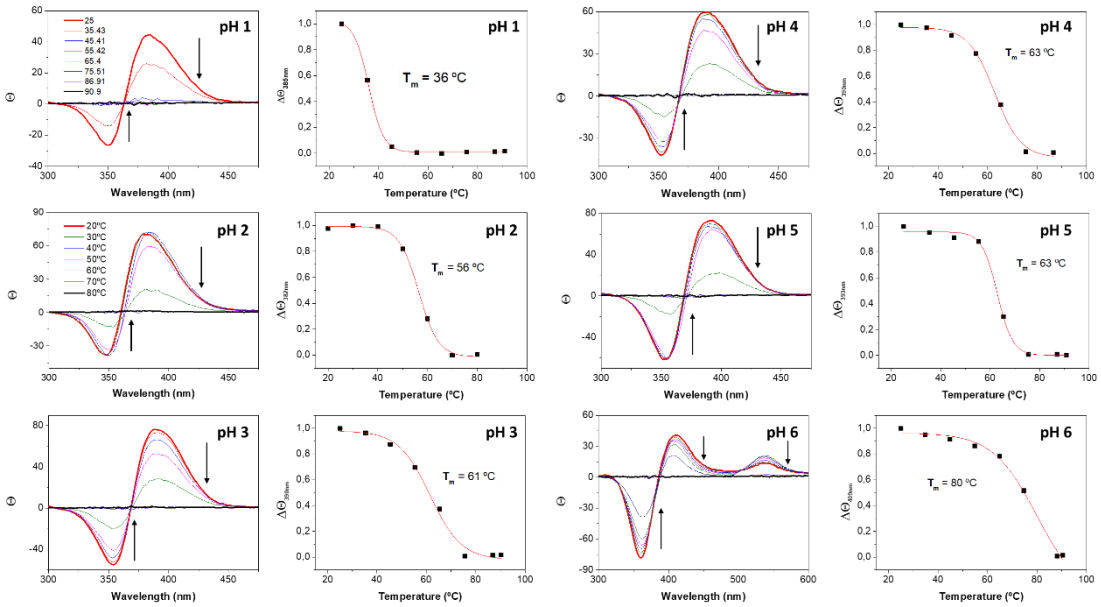

Fig. S58. Monitoring of hydrogels disassembly with temperature by CD from 25-95 ºC. Melting temperature (Tm) determination by plotting molar ellipticity (wavelength of the positive band of exciton coupling) versus temperature.

S15. UV-vis monitoring of gelation at pH 1.

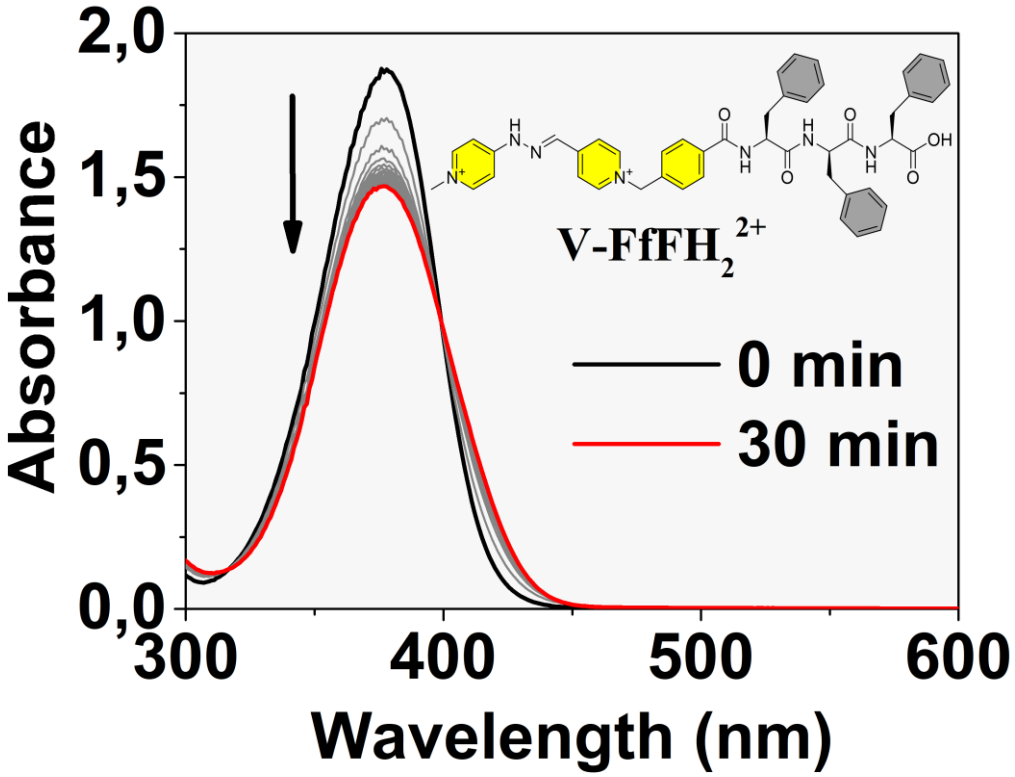

Fig. S59. Spectra recorded over time of the gelation of **V-FfF**H_2·2Cl at 5 mM in phosphate buffer at pH 1.

S16. Characterization of 5-FU@V-FfFH$^+$.

Oscillatory rheology measurements were conducted using same experimental conditions described in section **S6**. All experiments were done in triplicate. A mean value of (29.0 ±20.7)x10^3 Pa and 132±112 Pa were obtained for the elastic modulus and stress respectively.

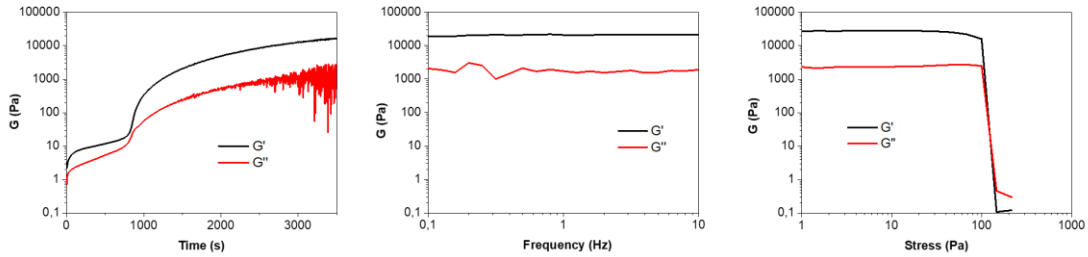

Fig. S60. Oscillatory rheometry time, frequency and stress sweeps experiments of 5-FU@**V-FfF**H$^+$ hydrogel.

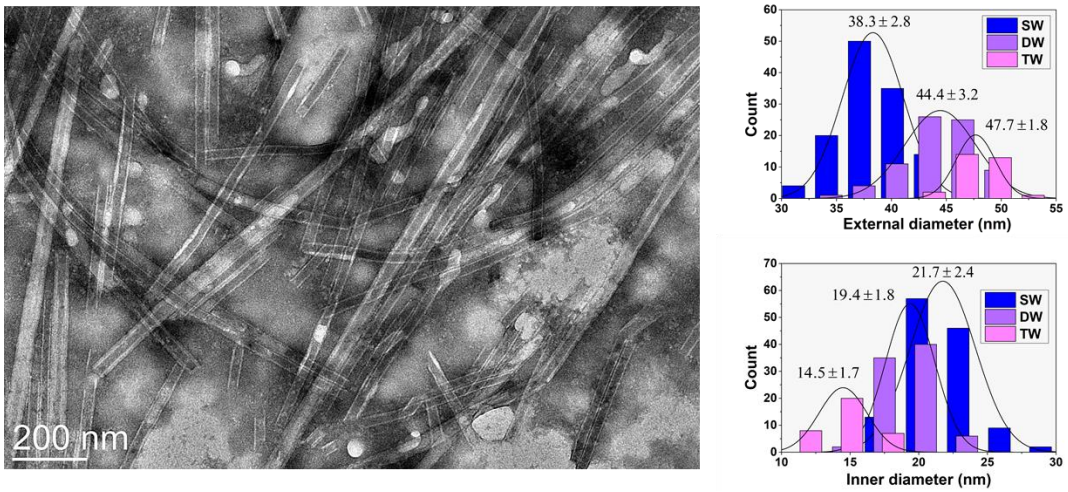

Fig. S61. TEM image of 5-FU@**V-FfF**H$^+$ and distribution of inner and external diameter of single (SW), double (DW) and triple (TW) nanotubes.

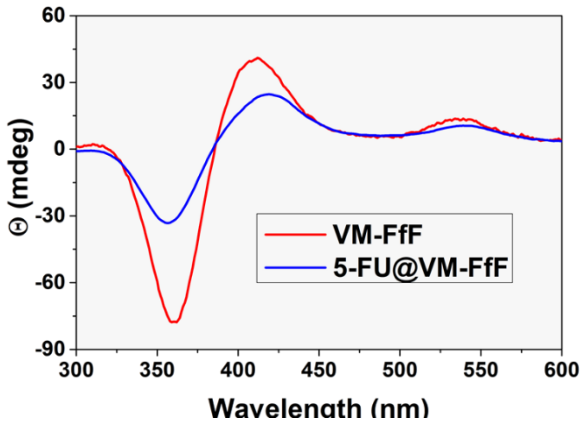

Fig. S62. Comparison of CD spectra of **V-FfF**H$^+$ and 5-FU@**V-FfF**H$^+$ hydrogels at 5 mM.

S17. Drug Release Studies.

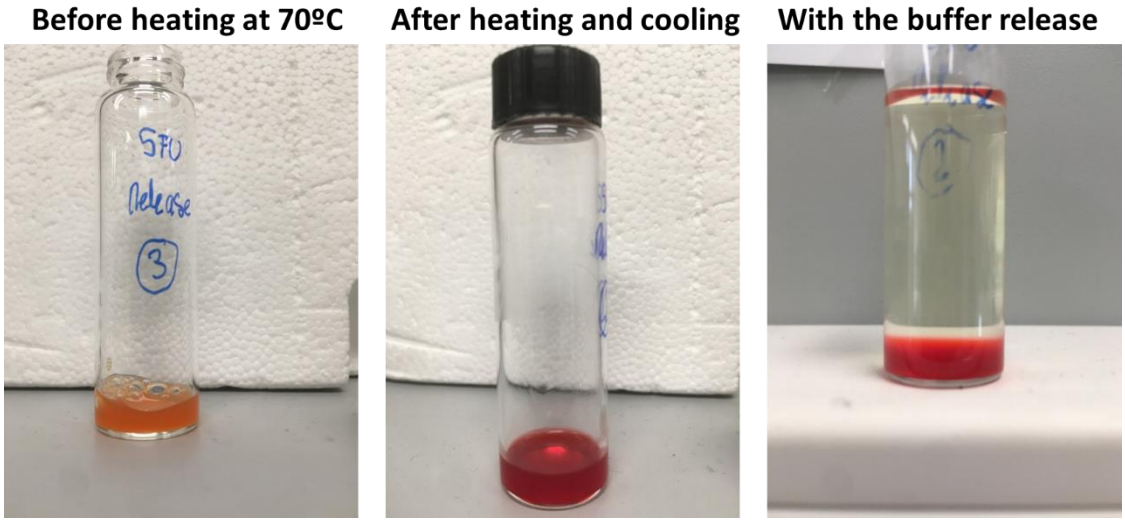

Fig. S63. Images of the preparation process of the **V-FfF**H_2·2Cl and 5-FU mixture at pH 6 (left image), hydrogel formed with 5-FU after heating to 70 °C and subsequently cooling to room temperature (center image), and hydrogel with the release buffer (right image).

To quantify the cumulative release of 5-FU, HPLC analysis was performed using an Agilent 1260 Infinity system equipped with a C18 column (Luna, 5 µm, 100 Å, 150 × 2 mm², Phenomenex). A gradient elution was applied using acetonitrile (MeCN)/water containing 0.1% formic acid as follows: 0–2 min, 5% MeCN; at 13 min, 95% MeCN; 13–15 min, 95% MeCN. The retention time (Rt) for 5-FU was 2 minutes. A calibration curve was first established over the concentration range of 0.01–0.25 mg/mL. The resulting calibration showed a slope of 75712.5 ± 826.0 A·mg/mL and an intercept of 101.4 ± 47.5. Immediately before each injection, 50 µL of release buffer were diluted to 250 µL with Milli-Q water to prevent detector saturation. **Table S2** lists, for every sampling time and replicate, the peak area, the 5-FU concentration (mg/mL) in the total release-buffer volume (8 mL), the cumulative release (%), and the mean cumulative release ± SD calculated from the three replicates.

Table S2. Results obtained from HPLC analysis of 5-FU release in replicates **S1**, **S2** and **S3** over time.

	S1			S2			S3			Average %
t/h	Area	mg/ml (8mL)	%	Area	mg/ml (8mL)	%	Area	mg/ml (8mL)	%	(SD)
0,1	1123,8	0,0675	10,8	850,6	0,0495	7,9	1473,0	0,0906	14,5	11,0 (3,3)
0,5	2309,7	0,1463	23,3	1376,9	0,0845	13,5	1931,1	0,1214	19,3	18,8 (5,0)
1	2772,3	0,1777	28,2	2200,0	0,1394	22,2	2689,7	0,1722	27,3	26,1 (3,3)
2	4189,9	0,2724	43,2	2940,5	0,1892	30,0	3328,0	0,2155	34,1	36,1 (6,8)
4	4751,3	0,3112	49,1	3737,0	0,2430	38,4	4051,0	0,2646	41,7	43,6 (5,6)
6	5946,1	0,3920	61,8	4920,5	0,3226	50,9	5376,6	0,3537	55,7	56,9 (5,5)
8	7602,2	0,5038	79,3	5871,9	0,3874	61,0	6290,9	0,4163	65,4	69,6 (9,7)
24	8250,7	0,5497	86,1	8326,3	0,5519	86,9	8068,8	0,5362	84,2	87,2 (1,4)
48	8125,0	0,5448	84,8	8571,6	0,5715	89,5	8233,7	0,5504	85,9	88,8 (2,2)
72	8386,1	0,5653	87,5	8781,8	0,5889	91,7	8616,3	0,5790	90,0	92,3 (1,9)
144	8689,2	0,5888	90,7	8458,7	0,5711	88,3	7883,3	0,5342	82,2	90,2 (4,4)
171	8298,6	0,5665	86,6	8502,2	0,5774	88,8	7736,1	0,5276	80,7	89,0 (4,2)

S18. Cell viability studies.

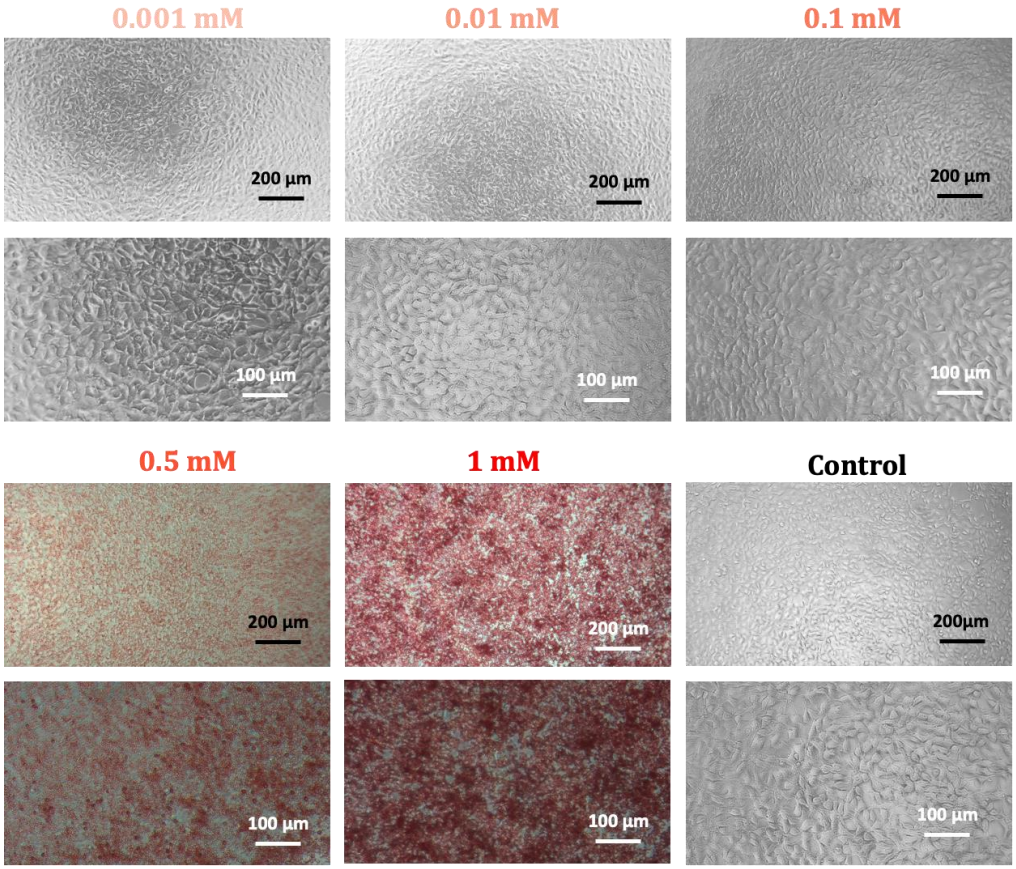

Fig. S64. Contrast phase microscopy images of NIH-3T3 cells grown on the tissue culture microwell plate and incubated with increasing concentrations of **V-FfF**H_2·2Cl.

S19. Critical aggregation concentration (CAC) for V-FfFH_2·2Cl at pH 7.

With the aim of correlating the effect of **V-FfF**H_2·2Cl concentration with the results obtained in the cell viability studies, the CAC of **V-FfF**H_2·2Cl at pH 7 was determined by circular dichroism (CD), following the aggregation-induced CD band in the 300–450 nm range.

Since the DMEM culture medium used for the cytotoxicity assays contains numerous CD-active components (amino acids, vitamins, nucleotides, etc.) that cause instability in both the baseline and the CD signal, we chose to use 0.1 M phosphate buffer at pH 7. This buffer provides the closest accessible pH to that of DMEM while allowing reliable CD measurements.

A series of **V-FfF**H_2·2Cl solutions in phosphate buffer at pH 7 was prepared at concentrations ranging from 5 to 0.1 mM (**Fig. S65**). After resting for 24 h, their CD spectra were recorded (**Fig. S66**).

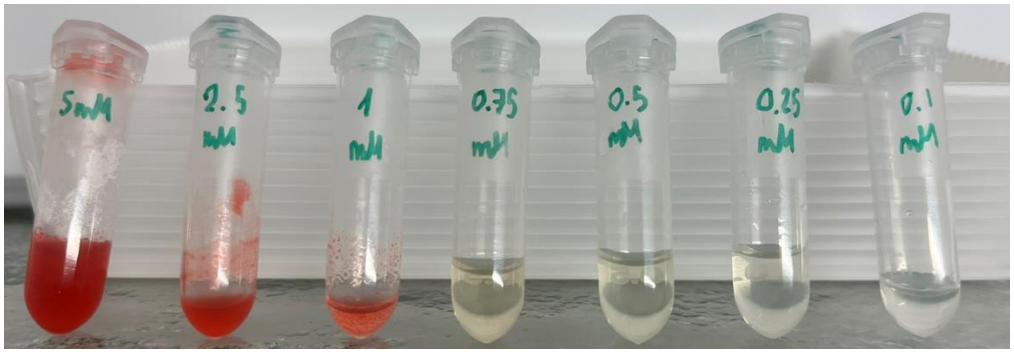

Fig. S65. Image of **V-FfF**H_2·2Cl mixtures at different concentrations in phosphate buffer at pH 7.

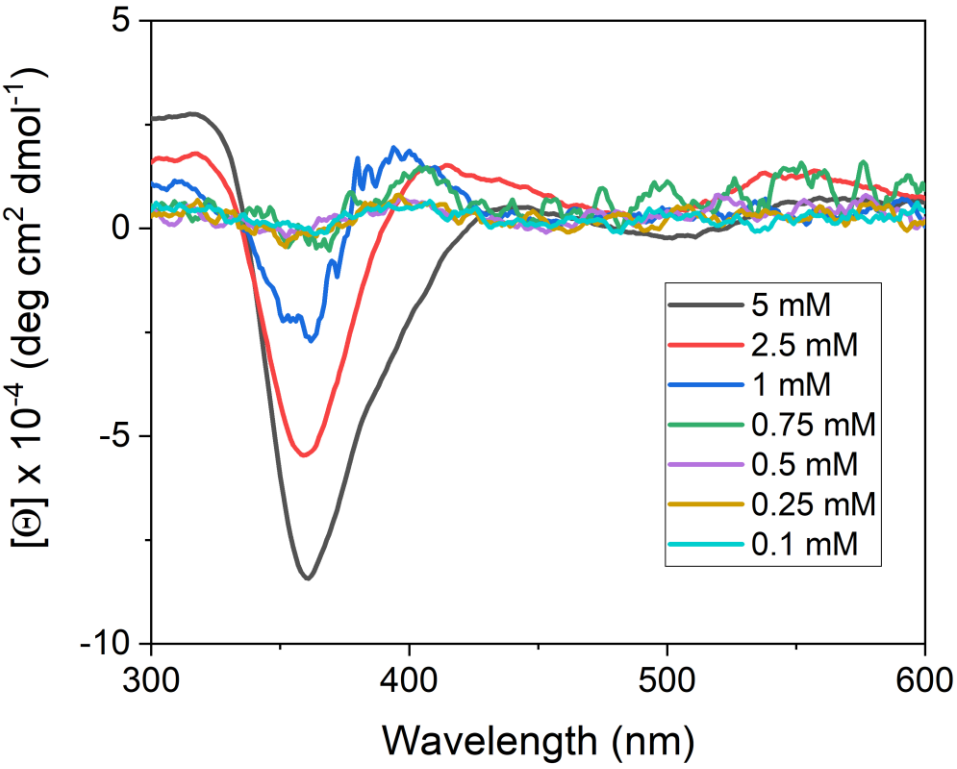

Fig. S66. CD spectrum of **V-FfF**H_2·2Cl at pH 7 recorded at different concentrations, showing the progressive disappearance of the CD band at 360 nm around 0.75 mM, signal associated with the self-assembly of the pseudopeptide.